Ultraviolet spectra of extreme nearby star-forming regions - approaching a local reference sample for JWST

Peter Senchyna, Daniel P. Stark, Alba Vidal-García, Jacopo Chevallard, Stéphane Charlot, Ramesh Mainali, Tucker Jones, Aida Wofford, Anna Feltre, Julia Gutkin

Monthly Notices
of the
ROYAL ASTRONOMICAL SOCIETY

MNRAS **472,** 2608–2632 (2017)
Advance Access publication 2017 August 16

doi:10.1093/mnras/stx2059

Ultraviolet spectra of extreme nearby star-forming regions – approaching a local reference sample for *JWST*

Peter Senchyna,[1]★ Daniel P. Stark,[1] Alba Vidal-García,[2] Jacopo Chevallard,[3] Stéphane Charlot,[2] Ramesh Mainali,[1] Tucker Jones,[4,5]† Aida Wofford,[6] Anna Feltre[7] and Julia Gutkin[2]

[1]*Steward Observatory, University of Arizona, 933 N Cherry Ave, Tucson, AZ 85721, USA*
[2]*Sorbonne Universités, UPMC-CNRS, UMR7095, Institut d'Astrophysique de Paris, F-75014 Paris, France*
[3]*Scientific Support Office, Directorate of Science and Robotic Exploration, ESA/ESTEC, Keplerlaan 1, NL-2201 AZ Noordwijk, the Netherlands*
[4]*Department of Physics, University of California Davis, 1 Shields Avenue, Davis, CA 95616, USA*
[5]*Institute for Astronomy, University of Hawaii, 2680 Woodlawn Drive, Honolulu, HI 96822, USA*
[6]*Instituto de Astronomía, UNAM, Ensenada, CP 22860, Baja California, Mexico*
[7]*Centre de Recherche Astrophysique de Lyon, Université Lyon 1, 9 Avenue Charles André, F-69561 Saint Genis Laval Cedex, France*

Accepted 2017 August 4. Received 2017 August 4; in original form 2017 June 2

ABSTRACT

Nearby dwarf galaxies provide a unique laboratory in which to test stellar population models below $Z_\odot/2$. Such tests are particularly important for interpreting the surprising high-ionization ultraviolet (UV) line emission detected at $z > 6$ in recent years. We present *HST*/*COS* UV spectra of 10 nearby metal-poor star-forming galaxies selected to show He II emission in SDSS optical spectra. The targets span nearly a dex in gas-phase oxygen abundance ($7.8 < 12 + \log \mathrm{O/H} < 8.5$) and present uniformly large specific star formation rates (sSFR $\sim 10^2$ Gyr^{-1}). The UV spectra confirm that metal-poor stellar populations can power extreme nebular emission in high-ionization UV lines, reaching C III] equivalent widths comparable to those seen in systems at $z \sim 6$–7. Our data reveal a marked transition in UV spectral properties with decreasing metallicity, with systems below $12 + \log \mathrm{O/H} \lesssim 8.0$ ($Z/Z_\odot \lesssim 1/5$) presenting minimal stellar wind features and prominent nebular emission in He II and C IV. This is consistent with nearly an order of magnitude increase in ionizing photon production beyond the He^+-ionizing edge relative to H-ionizing flux as metallicity decreases below a fifth solar, well in excess of standard stellar population synthesis predictions. Our results suggest that often-neglected sources of energetic radiation such as stripped binary products and very massive O-stars produce a sharper change in the ionizing spectrum with decreasing metallicity than expected. Consequently, nebular emission in C IV and He II powered by these stars may provide useful metallicity constraints in the reionization era.

Key words: stars: massive – galaxies: evolution – galaxies: stellar content – ultraviolet: galaxies.

1 INTRODUCTION

The first deep spectra of galaxies at $z > 6$ present a striking contrast to the properties of typical star-forming galaxies at lower redshift. Ground-based spectroscopy probing the rest frame ultraviolet (rest-UV) of gravitationally lensed Lyman-α emitters at $z > 6$ has revealed nebular emission in transitions of highly ionized species including C^{2+}, O^{2+} and C^{3+} (Stark et al. 2015a,b, 2017; Mainali et al. 2017). The observed equivalent width of C III] and O III] exceeds that seen in typical UV-selected star-forming galaxies at $z \sim 2$–3 by an order of magnitude, and nebular C IV is rarely seen in emission at all in these or local star-forming samples. Studies with ALMA targeting [C II] and [O III] emission and with *Spitzer* probing rest-optical nebular line excesses in broad-band photometry at $z > 6$ paint a similar picture, suggesting that extreme radiation fields are more common in star-forming galaxies at these early times (see Stark 2016 for a review).

The rest-UV properties of these objects are not entirely without precedent in lower-z samples. For instance, nebular C IV and He II emission (requiring flux beyond ∼50 eV) is seen in some lensed

★ E-mail: senchp@email.arizona.edu
† Hubble Fellow.

star-forming dwarf galaxies at $z \sim 2$–3 (Erb et al. 2010; Christensen et al. 2012; Stark et al. 2014; Vanzella et al. 2016, 2017). This suggests that the additional ionizing flux may be provided by low-metallicity stars. Rest-optical spectroscopy of galaxies at $z \sim 2$–3 has also revealed differences with respect to models calibrated at near-solar metallicity. In particular, offsets in diagnostic line ratios have been interpreted as due to some combination of higher nitrogen abundance and harder ionizing radiation fields at these redshifts (e.g. Kewley et al. 2013; Steidel et al. 2014; Shapley et al. 2015; Sanders et al. 2016; Kashino et al. 2017; Kojima et al. 2017; Strom et al. 2017).

Indeed, these surprising detections at high-z were presaged by spectroscopy of low-metallicity dwarf galaxies in the nearby universe. Detections of nebular He II λ4686 emission in nearby stellar-photoionized H II regions date back to at least 1985, and its origin remains mysterious (e.g. Garnett et al. 1991; Thuan & Izotov 2005; Brinchmann, Kunth & Durret 2008b; Shirazi & Brinchmann 2012; Kehrig et al. 2015). The nebular He II λ1640 and 4686 lines are emitted in the cascading recombination of He^{++}, produced by ionizing photons beyond 54.4 eV. Due to strong absorption in the atmospheres and winds of massive stars, even very hot stellar models considered in standard population synthesis prescriptions generally predict very few photons in this energy range. The necessary ionizing flux has thus been attributed variously to very massive stars, high-mass X-ray binaries and fast radiative shocks.

UV spectra of nearby star-forming regions are far less ubiquitous than optical spectra, but previous UV work also hints at some commonalities with extreme high-z galaxies. The *International Ultraviolet Explorer* satellite (*IUE*; e.g. Kinney et al. 1993; Giavalisco, Koratkar & Calzetti 1996; Heckman et al. 1998, and references therein) as well as the Goddard High Resolution Spectrograph (*GHRS*) and Faint Object Spectrograph (*FOS*) previously onboard the *Hubble Space Telescope* (*HST*; Garnett et al. 1995; Leitherer et al. 2011) enabled a detailed study of rest-UV stellar and nebular features in local star-forming galaxies. Data from these instruments reveal that the [C III], C III] λλ1907, 1909 semi-forbidden doublet (hereafter C III] doublet) reaches extremely high equivalent widths in a handful of systems below half-solar metallicity, but does not appear to follow a monotonic trend with gas-phase oxygen abundance or Lyα equivalent width (e.g. Bayliss et al. 2014; Rigby et al. 2015). Further interpretation of these data is complicated by the limited resolution and sensitivity of these UV spectrographs and by the small number of metal-poor objects with archival coverage.

Observations of both nearby massive stars and peculiar galaxies in the distant universe have motivated a great deal of work in both stellar modelling and stellar population synthesis. Models of the atmospheres and winds of massive stars have advanced considerably in the past decades, incorporating non-LTE effects and full hydrodynamical modelling of winds, with substantial effects on the predicted emergent ionizing flux (e.g. Kudritzki, Pauldrach & Puls 1987; Pauldrach, Hoffmann & Lennon 2001; Smith, Norris & Crowther 2002; Todt et al. 2015). The incorporation of physics such as stellar rotation (e.g. Maeder & Meynet 2000; Levesque et al. 2012; Szécsi et al. 2015) and binary mass transfer (e.g. Eldridge, Izzard & Tout 2008; de Mink et al. 2014; Gotberg, de Mink & Groh 2017) has significant effects on the evolution of individual stars, and both tend to enhance the ionizing flux produced by composite stellar populations (e.g. fig. 2 of Wofford et al. 2016). Much progress has also been made in self-consistently predicting the emergent stellar continuum and nebular emission of galaxies and linking spectral observations to underlying physical parameters of interest (e.g. Charlot & Longhetti 2001; Eldridge & Stanway 2009; Chevallard & Charlot 2016; Gutkin, Charlot & Bruzual 2016; Byler et al. 2017; Leja et al. 2017; Vidal-García et al. 2017, Charlot & Bruzual 2017, in preparation). However, the calibration of all components of these models is most challenging at the low metallicities expected in the reionization era.

The relatively common detection of high-ionization emission at $z > 6$ and in star-forming dwarf galaxy populations nearby suggest a substantial evolution in the ionizing spectra of stellar populations with metallicity. Empirical constraints on stellar models at low metallicities are difficult to obtain. Individual stars can only be resolved reliably within the Local Group, and thus direct calibration of massive star models extends down only to approximately $Z/Z_{\odot} \sim 1/5$, or $12 + \log \mathrm{O/H} \sim 8.0$ (see e.g. Massey 2003; Garcia et al. 2014; Bouret et al. 2015; Crowther et al. 2016). Comprehensive tests of stellar population models at the highest masses and lowest metallicities require high-sSFR populations outside the Local Group, and detailed spectroscopy of weak nebular lines and stellar features in integrated light spectra of individual systems is generally only possible at low redshift (see e.g. Leitherer et al. 2011; Wofford et al. 2014). The metal-poor dwarf galaxy population nearby (within a few hundred Mpc) is thus a critical laboratory in which to test stellar population synthesis models at sub-SMC metallicities.

However, locating and studying local galaxies with UV emission comparable to that seen in $z > 6$ systems have proved challenging. In particular, no nearby star-forming galaxies with nebular C IV approaching the ∼20–40 Å observed at $z \sim 6$–7 (Stark et al. 2015b; Mainali et al. 2017) have yet been identified. Previous local UV spectroscopic samples have focused on Lyα, the UV slope, and C/O as probed via the C III] and O III] doublets (e.g. Garnett et al. 1995; Giavalisco et al. 1996; Leitherer et al. 2011; Berg et al. 2016). While sufficient to reveal that C III] equivalent widths do reach ∼20 Å in some metal-poor galaxies (Rigby et al. 2015), these observations lack the coverage and resolution necessary to study the most extreme UV lines. Measuring C IV and He II especially at low equivalent width requires sufficient resolution to disentangle nebular emission from broad stellar wind lines and interstellar absorption, and thus all but the strongest nebular emission is difficult to constrain with *FOS* and *COS* (Cosmic Origins Spectrograph) low-resolution gratings ($R \equiv \lambda/\Delta\lambda \lesssim 2000$, unbinned). Archival samples are also biased towards relatively high metallicities; the *FOS*/*GHRS* atlas compiled by Leitherer et al. (2011) contains only six galaxies below $12 + \log \mathrm{O/H} \lesssim 8.0$. In order to study nebular line production and constrain the associated stellar populations, we require large samples of metal-poor galaxies (necessarily probing to fainter objects) with moderate resolution spectral coverage. The *COS* installed by *HST* Servicing Mission 4 now provides the sensitivity and medium-resolution gratings ($R > 16\,000$, unbinned) necessary to begin this work in-earnest.

We have undertaken a campaign to investigate the stellar populations and physical conditions which power high-ionization nebular emission locally. In Cycle 23 (GO: 14168, PI: Stark) we obtained *HST*/*COS* UV spectra of 10 star-forming galaxies selected to have He II λ4686 emission in optical SDSS spectra (Shirazi & Brinchmann 2012). This emission is indicative of the hard $\gtrsim$50 eV radiation necessary to power UV high-ionization lines. Grating settings were selected to constrain the full suite of high-ionization UV lines detected at high-z: C IV, He II, O III] and C III]. The galaxies were chosen to span nearly a dex in gas-phase metallicity $7.6 \lesssim 12 + \log \mathrm{O/H} \lesssim 8.4$ (roughly $1/10 < Z/Z_{\odot} < Z/2$) in order to explore the metallicity dependence of the UV spectra. We discuss the sample and data

Table 1. Basic properties and *HST*/*COS* exposure times for our 10 targets.

SBID	RA (J2000)	Dec (J2000)	Wolf–Rayet class from SDSS (SB2012)	Distance (Mpc)	2.5 arcsec comoving kpc	u, i AB mag	NUV/G185M, FUV/G160M exposure (s)
2	9:44:01.87	−0:38:32.2	Non-WR	19	0.23	18.2, 18.1	2168, 2577
36	10:24:29.25	5:24:51.0	Non-WR	141	1.71	18.1, 18.0	2136, 2609
80	9:42:56.74	9:28:16.2	WR	46	0.56	17.9, 18.1	2132, 2608
82	11:55:28.34	57:39:52.0	Non-WR	76	0.92	18.0, 18.0	2344, 2853
110	9:42:52.78	35:47:26.0	Non-WR	63	0.76	18.2, 18.4	2156, 2665
111	12:30:48.60	12:02:42.8	WR	16	0.20	18.5, 18.4	2132, 2613
179	11:29:14.15	20:34:52.0	WR	25	0.30	18.3, 18.5	2160, 2588
182	11:48:27.34	25:46:11.8	Non-WR	191	2.31	18.3, 17.9	2112, 2625
191	12:15:18.60	20:38:26.7	WR	10	0.12	17.7, 18.2	2156, 2616
198	12:22:25.79	4:34:04.8	Non-WR	16	0.20	18.3, 18.8	2120, 2605

in more detail in Section 2. In Section 3, we present the *HST*/*COS* UV spectra in the context of the optical measurements. We describe first results from stellar population synthesis fits to the full UV spectra in Section 4, to be continued in a follow-up paper (Chevallard et al., in preparation). We then discuss implications for high-redshift observations and stellar population synthesis at low-metallicities in Section 5, and conclude in Section 6.

We assume a solar oxygen abundance of $12 + \log_{10}([\mathrm{O/H}]_{\odot}) = 8.69$ (Asplund et al. 2009). For distance calculations and related quantities, we adopt a flat cosmology with $H_0 = 70\ \mathrm{km\,s^{-1}\,Mpc^{-1}}$.

2 SAMPLE SELECTION AND DATA

2.1 SDSS galaxies with He II emission

To find a set of metal-poor galaxies with hard ionizing stellar spectra, we rely on the detection of diagnostic lines in SDSS optical spectra. Shirazi & Brinchmann (2012, SB2012 hereafter) searched the SDSS DR7 spectral data base (York et al. 2000; Abazajian et al. 2009; Ahn et al. 2012) for nebular He II λ4686 emission. This helium recombination line (technically a blended multiplet) is indicative of a very hard ionizing continuum, as the energy required to strip He^+ of its one electron is 54.4 eV (λ ≃ 228 Å).

The SDSS DR7 spectroscopic sample consists of all objects targeted in SDSS I and II. Ignoring the stars and supernovae targeted as part of SDSS-II (SEGUE and the SDSS Supernova Survey), this sample is equivalent to the SDSS Legacy survey. The SDSS Legacy Survey selected galaxies, quasars and luminous red galaxies for spectroscopic follow-up by making a variety of photometric cuts (Eisenstein et al. 2001; Richards et al. 2002; Strauss et al. 2002). In particular, the main galaxy sample is estimated to be complete to >99 per cent for all galaxies in the SDSS footprint with r-band Petrosian magnitudes $r \leq 17.77$ and half-light surface brightnesses $\mu_{r,50} \leq 24.5\ \mathrm{mag\,arcsec^{-2}}$ (Strauss et al. 2002). In total, the sample contains ∼1.5 million spectra collected over ∼8000 $\mathrm{deg^2}$. While the SDSS spectroscopic sample is not complete to all dwarf galaxy morphologies (see e.g. James et al. 2015), our selection goal was to identify metal-poor objects sufficiently bright and compact for *HST*/*COS* follow-up.

In order to separate active galactic nuclei (AGN) from predominantly star-forming galaxies, SB2012 employed a range of line ratio diagnostics. Shirazi & Brinchmann required an S/N > 3 detection of Hβ, [O III] λ5007, Hα, and [N II] λ6584 so as to enable a traditional Baldwin, Phillips & Terlevich (1981, BPT) diagram analysis. In addition, nebular line diagnostics incorporating He II were used to place firmer constraints on the hardness of the ionizing spectrum and minimize contamination from AGN. This analysis identified 2865 He II detections with line widths comparable to the strong forbidden and recombination lines, and 189 with line ratios, indicating a predominantly stellar ionizing spectrum.

The final SB2012 star-forming subsample is overwhelmingly nearby, with the vast majority located at $z < 0.1$. The objects span the metallicity range $7.5 < 12 + \log_{10}(\mathrm{O/H}) < 9.5$. They range in character from H II regions embedded in larger galaxies to isolated blue compact dwarfs.

We selected 10 of these star-forming He II-emitters to target with *HST*/*COS* UV spectroscopy in the *HST* program GO 14168 (PI: Stark). Our primary goal was identifying moderately metal-poor ($12 + \log_{10}(\mathrm{O/H}) \sim 7.7$–$8.2$, i.e. $Z/Z_{\odot} \sim 1/8$–$1/3$) objects with intense radiation fields. Thus, we selected targets spread evenly throughout this range. We utilized the gas phase metallicity estimates produced by SB2012 who used the grid of photoionization models described by Charlot & Longhetti (2001) to fit the measured emission line fluxes.

In addition, we selected targets such that approximately half showed signs of Wolf–Rayet (WR) stars in the optical according to SB2012. These stellar wind signatures are the broad blue and red wind emission bumps located near 4650 and 5808 Å, respectively, consisting of blended He II λ4686, C IV λλ5801 − 12, and various metal lines (e.g. Crowther 2007). While WR stars have been suggested as the most likely stellar population to produce the hard ionizing spectrum required for nebular He II emission, previous studies have found an unclear association between this nebular emission and the WR wind bumps at low metallicity (e.g. Guseva, Izotov & Thuan 2000; Brinchmann, Kunth & Durret 2008b; Shirazi & Brinchmann 2012).

The targets selected for *HST*/*COS* observation (see Table 1) reside in a variety of environments, from isolated dwarf galaxies to H II regions embedded in larger disc systems, and range in distance from ∼10to 200 Mpc. The final sample of 10 is listed in Table 1, and SDSS cutouts for each are plotted in Fig. 1. To estimate distances, we adopt the local velocity flow model described by Tonry et al. (2000) with $H_0 = 70\,\mathrm{km\,s^{-1}\,Mpc^{-1}}$ and check the literature for more robust measurements. The uncertainty in redshift-only distance estimates is dominated by the random motion of galaxies and by systematic error arising from group assignment. The inverse model relating observed recessional velocity to distance does not have a unique solution for objects near the Virgo cluster. In cases where the sky position and redshift are consistent with Virgo, and no other literature distances or group assignments are available, we assume a distance of 16.5 Mpc (Mei et al. 2007). A case-by-case distance analysis is presented in Appendix A. Uncertainty in the process of distance assignment in this work translates mainly

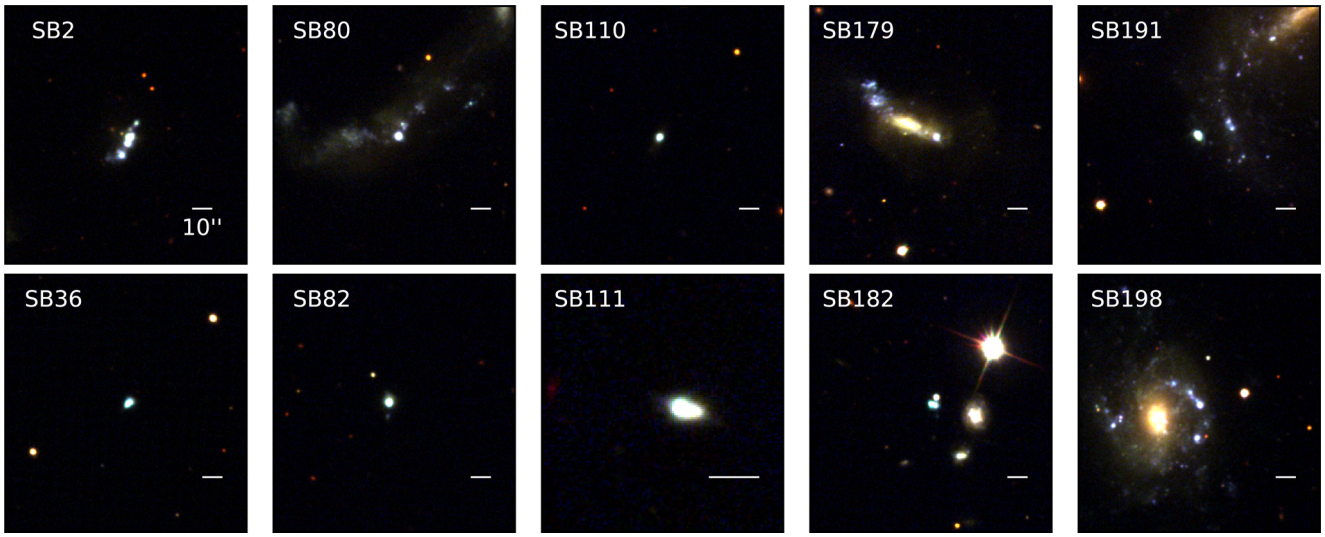

Figure 1. SDSS *u*, *g*, *r* montage images centred on our targets. The scale bar is fixed at 10 arcsec in length (SB111 is zoomed in to avoid the edge of the SDSS frame). The objects span a range of environments, from isolated dwarfs to H II regions embedded in larger galaxies.

into potential systematic uncertainty in inferred stellar masses and absolute star formation rates.

Since this work is primarily concerned with understanding the UV spectra of young star-forming regions, we focus our analysis on the *HST*/*COS* aperture. At these distances, the projected *HST*/*COS* aperture radius corresponds to physical scales ranging from 60 to 1200 pc, but the star formation rate and stellar mass surface densities within this aperture span a much smaller dynamic range (see Section 3). The bulk properties of the galaxies in which several of our objects are embedded likely have negligible direct impact on the emergent spectra of the star-forming regions within the *HST*/*COS* aperture, and thus are beyond the scope of this paper.

Selecting systems by high-ionization line emission such as in He II may result in a bias towards systems with unusual IMF sampling. As found in Section 3.1, the masses and star formation rates ($\gtrsim 10^{4.7}\,M_\odot$ and $\gtrsim 10^{-2}\,M_\odot\,yr^{-1}$) of our sample are above the range where stochastic sampling of the IMF has been previously inferred to significantly impact UV and Hα emission (e.g. Lee et al. 2009). However, the impact of stochastic sampling on stellar wind features and the >54.4 eV continuum is less clear. We do not expect IMF sampling to have a significant impact on our interpretation of trends in our sample beyond potentially introducing scatter, but future work considering these effects will be important especially for detailed comparisons with stellar population synthesis models (Vidal-García et al., in preparation).

2.2 *HST*/*COS*

The *HST*/*COS* observations were performed in the NUV at ∼1910 Å (with the G185M grism) and the FUV targeting 1450–1700 Å (G160M) with the 2.5 arcsec diameter Primary Science Aperture (PSA). These grisms provide an optimal balance between spectral resolution and wavelength coverage for our program. The observations are described in Table 1. Wavelength settings were chosen for each target to provide rest-frame coverage of [C III] 1907, C III] 1909 Å; O III] λλ1661, 1666; He II 1640; and C IVλλ1548, 1550. The targets were acquired in ACQ/IMAGE mode with MIRRORA and 43–95 s exposures (adjusted for the *GALEX*/NUV flux of each target). The target acquisition images are displayed in Fig. 2.

The data were taken in TIME-TAG mode with FP-POS=ALL and FLASH=YES. These settings allow a flat image to be constructed and minimize the impact of fixed-pattern noise in the detectors. The data were reduced using CALCOS 3.1.7 (2016-02-03) and the latest calibration files (as of 2016-07-01) downloaded using STSDAS.

Extraction was performed using the default parameters for each detector. The NUV extraction is performed using the BOXCAR algorithm by default; we confirmed that all target flux visible in the 2D NUV corrtag spectra was within the default extraction box. As our targets are not point sources, we checked to ensure that the FUV TWOZONE extraction (optimized for point sources) was collecting all available target flux. To do so, we re-ran the FUV extractions with the BOXCAR algorithm after checking to ensure that the box width captured the entirety of the target trace in the 2D corrtag spectra. The final 1D spectra extracted using these two methods were virtually indistinguishable, so we chose to use the preferred TWOZONE output for the FUV data.

The G160M and G185M gratings have dispersions of 12.23 and 34 mÅ pixel^{-1}; or (since the FUV XDL and NUV MAMA have 6 and 3 pixels per resolution element) 73.4 and 102 mÅ resolution element. We checked the approximate attained resolution of the spectra by fitting narrow Milky Way absorption features. As these are much more common in the FUV/G160M wavelength range, most of our constraints come from this grism. These fits yield line σ (FWHM) of approximately 0.254 Å (0.598 Å) on average, corresponding to approximately 3.5 (8.1) resolution elements in the FUV and 2.5 (5.9) resolution elements in the NUV, respectively. The one-dimensional spectra are binned via boxcar averaging over the length of this resolution element (or a multiple thereof) to achieve higher S/N per pixel.

2.3 MMT

The redshifts of our sample shift [O II] λ3727 into the SDSS spectral range for only two galaxies. We obtained supplementary optical spectra for the other eight targets with the Blue Channel spectrograph on the MMT. These observations were made with the 1.5 x 180 arcsec slit and either the 800 or 300 lines mm^{-1} grating. The resulting 800 lpm (300 lpm, respectively) spectra have a dispersion of 0.75 (1.96) Å pixel^{-1}, a spectral FWHM resolution measured

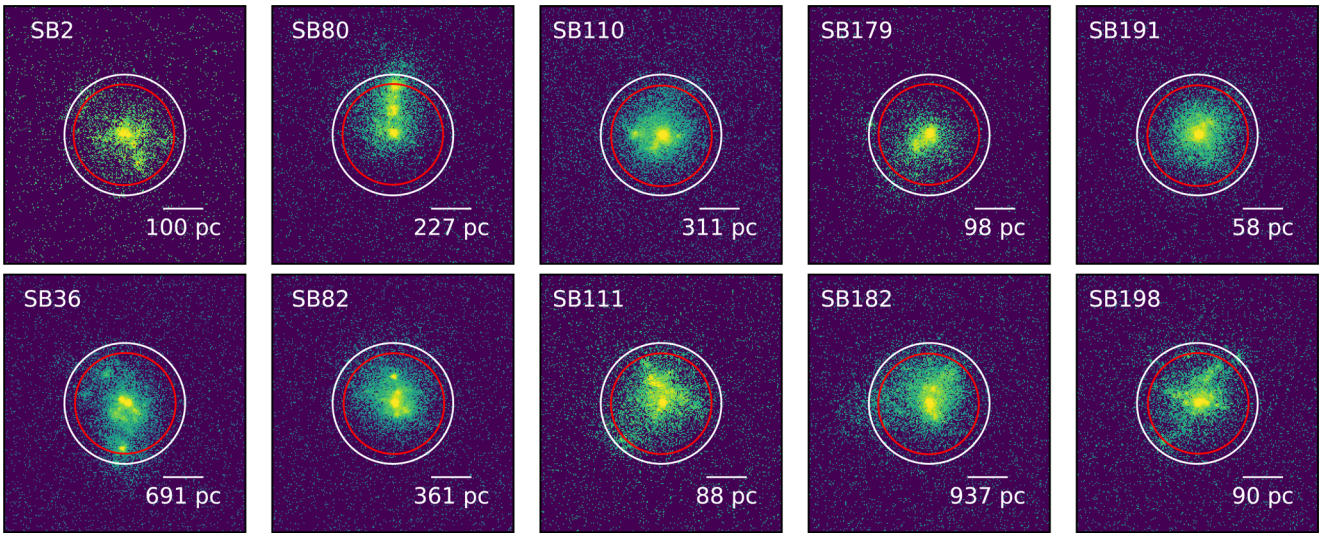

Figure 2. *HST*/*COS*NUV/MIRRORA target acquisition images. The white circle in each represents the SDSS 3 arcsec fibre aperture centred on the SDSS coordinates of the target; and the red circle represents the *COS* 2.5 arcsec aperture after centring on the flux centroid of the image. The 1 arcsec scalebar is labelled with an estimate of the comoving distance corresponding to this angle at the redshift of each target.

Table 2. Log of MMT observations from the nights of 2016 January 20 and 2017 January 8.

SBID	Airmass	Exposure (s)
	2016 January 20	
80	1.2	4500
2	1.2	2833
	2017 January 8	
179	1.1	1200
110	1.1	1200
82	1.2	1200
191	1.0	900
198	1.1	1200
111	1.0	1500

from the [O III] lines of approximately 3.3 (6.9) Å, a spatial scale of ∼0.6arcsec pixel along the slit, and all cover the wavelength range 3200–5200 Å. Data for SB2 and 80 were taken on the night of 2016 January 20 with the 800 lpm grating at airmass $\lesssim$1.5 and with (guider) seeing ranging from 0.9 to 1.5 arcsec. The targets SB 179, 110, 82, 191, 198 and 111 were observed in the second half of the night of 2017 January 8 with the 300 lpm grating at airmass $\lesssim$1.2; seeing reported by the guider remained near 1 arcsec. Arcs were obtained for each target with the HeAr and HgCd lamp combinations separately to cover the full observed wavelength range. Standard stars LB 227, GD 108 and Feige 66 were observed at the beginning, middle and end of the night (respectively) on 2016 January 20 and Feige 34 was observed on 2016 January 8. Each target was observed at the parallactic angle to minimize slit loss. The observations are summarized in Table 2. The data were reduced with standard long-slit techniques in IRAF,[1] and strong line fluxes were compared with the SDSS measurements to obtain an effective aperture correction for each target.

[1] IRAF is distributed by the National Optical Astronomy Observatories, which are operated by the Association of Universities for Research in Astronomy, Inc., under cooperative agreement with the National Science Foundation.

Table 3. Log of ESI observations.

SBID	Airmass	Exposure (s)
	2016 March 29	
110	1.1	8100
82	1.3	9000
191	1.1	5400
198	1.4	4200
	2017 January 20	
2	1.6	7200
182	1.4	9000
111	1.1	8100
	2017 January 21	
80	1.3	6400
179	1.1	5400
36	1.2	9600

2.4 ESI

We also obtained data with the Echellette Spectrograph and Imager (ESI; Sheinis et al. 2002) on Keck II for our targets. These data were taken with the 1 × 20 arcsec slit on 2016 March 29 and 2017 January 20–21 under seeing ranging from ∼0.8 to 1.2 arcsec (see Table 3). This yields spectra covering the wavelength range 3900–10900 Å with approximately 11.5 km s^{-1} pixel^{-1} dispersion and 0.154 arcsec pixel^{-1} along the slit.

We reduced the ESI spectra using the `ESIRedux` code.[2] Dome flats and HgNeXeCuAr lamp exposures were used to perform flat and wavelength calibrations. The object continuum was used to trace the echelle orders in each exposure, and the spectra were boxcar-subtracted with a radius of 20 pixels to ensure that all object flux was captured. Since an archival sensitivity curve was used to perform first-order flux corrections, the final one-dimensional spectra are flux-calibrated only in a relative sense. These spectra yield an extremely high-resolution view of optical lines, which is critical in crowded line complexes such as that near He II λ4686.

[2] http://www2.keck.hawaii.edu/inst/esi/ESIRedux/

2.5 SDSS

Our targets were selected using optical fibre spectra and imaging originally released in SDSS DR7. We obtained reduced spectra and imaging frames for our objects from the SDSS archive. The spectra cover approximately the wavelength range 3800–9200 Å at a spectral resolution $R \sim 1800$. The fibre diameter is approximately 3 arcsec on- sky (York et al. 2000). Imaging from SDSS covers 5 filters denoted u, g, r, i and z, with central wavelengths ranging from 3551 to 8932 Å.

2.6 Line measurement and photometry

We use custom fitting software to measure line features in the one-dimensional spectra. For isolated emission and absorption lines, we adopt a model consisting of a linear function describing the local continuum plus a Gaussian described by a mean, total area and standard deviation. For close doublets and lines with potentially two different velocity components, we add a second Gaussian to this model (in the former case, with line widths enforced to be similar to the first). We define the Bayesian posterior likelihood function as the product of a χ^2 likelihood describing the data-model difference with a flat prior over physically plausible ranges of the model parameters. To infer parameter values given our model and data, we explore the resulting posterior distribution using the affine-invariant Markov chain Monte Carlo (MCMC) ensemble sampler EMCEE (Foreman-Mackey et al. 2013). After removing burn-in, we adopt the 16–50–84 percentiles from the sampler distribution as our parameter value and error estimates. These fits are initiated with parameters centred on a guess at the feature to be fit; we adjust burn-in and check the results visually to ensure that the chain has converged on a reasonable model and that the resulting likelihood functions are not significantly multimodal.

The spectroscopic apertures of *COS* and SDSS are roughly circular and of-order the same size (2.5 and 3 arcsec in diameter, respectively); thus aperture photometry is appropriate for analysis of the broad-band properties of the targets. We measure flux in the SDSS images using a 3-arcsec diameter circular aperture and estimate the local sky background within 1 arcmin after sigma-clipping (low 10σ, high 3σ).

2.7 Dust corrections

Correction of attenuation due to dust absorption and scattering is of paramount concern in the UV. The choice of attenuation model can have a significant effect on parameters inferred from UV spectral features (see e.g. Wofford et al. 2014). For fitting photometry and UV spectral features in this paper, we adopt the 2-component model presented by Charlot & Fall (2000), as described in Section 4.

For the purposes of correcting optical emission lines for dust attenuation in Section 3, we adopt a simplified approach. In particular, we utilize extinction curves rather than an attenuation model, as scattering should have a minimal effect in the optical over the small field of view probed by the SDSS aperture. First, we correct for Galactic dust extinction towards each object. Galactic extinction maps and curves are relatively well-determined; in particular, we use the maps of Schlafly & Finkbeiner (2011) to determine $E(B-V)$ and assume the $R_V = 3.1$ extinction curve of Fitzpatrick (1999). To estimate the residual intrinsic reddening of the nebular emission in each galaxy, we measure the Balmer decrement relative to the Case B recombination value of Hα/Hβ computed with `PyNeb` (Luridiana, Morisset & Shaw 2015) for the T_e and n_e values computed from [O III] with this software as described in Section 3.2 – we repeat the process of deriving n_e, T_e, and $E(B-V)$ until these quantities converge (which occurs within three iterations). The final adopted values of Hα/Hβ range from 2.78 to 2.86. We adopt the SMC bar average extinction curve measured by Gordon et al. (2003). The results for optical lines are essentially unchanged if we instead use the Galactic diffuse average curve of Fitzpatrick (1999), since these curves diverge significantly only in the UV. These systems are dominated by young stars such that correction of the Balmer lines due to underlying stellar absorption is negligible; the ESI data reveal underlying absorption in Hβ for only one system (SB 111) at 4 per cent of the total line flux.

For each object, we check that the extinction derived via the Balmer decrement is consistent with Case B predictions for the other Balmer lines accessible in the SDSS spectra (Hγ, Hδ). The agreement is good to within a few per cent and consistent with the measurement errors in the line ratios, except in the case of SB 2. The reddening inferred from Hα/Hβ yields Case B predictions for Hδ and Hγ which are very inconsistent with the observed values even accounting for reasonable variation in T_e. In addition, the Hα line profile for SB 2 shows an asymmetric redward extension which accounts for about half the total flux in the line and does not appear in the other strong nebular lines or in the ESI spectrum of this source. Ignoring Hα and instead using the ratio of Hβ/Hγ to de-redden the optical yields an intrinsic $E(B-V)$ in much better agreement with the other objects (cf. $\sim$0.5 using Hα/Hβ) and in good agreement with Hδ. For the purposes of measuring extinction and other properties of the nebular gas in this object, we ignore the raw Hα flux and instead predict it where necessary from Hβ/Hγ and Case B.

3 RESULTS

The UV spectra of star-forming systems are sensitive to both gas conditions as well as the winds and ionizing spectra of massive stars. In this section, we first present measurements and physical parameters derived from optical photometry and spectra. We then explore the *HST*/*COS* UV spectra in the context of these other measurements. Finally, we present the Keck/ESI optical spectra, which provide a close look at He II λ4686 and the WR stars in these systems.

3.1 Bulk stellar population constraints from photometry

The optical broad-band photometry provides constraints on the total stellar mass and star formation activity. We fit the SDSS photometry using the Bayesian spectral analysis code BEAGLE[3] (Chevallard & Charlot 2016); this code and the parameter space explored by the models are described in detail in Section 4. We adopt a constant star formation history for our analysis as this provides an adequate fit to the measurements. Incorporating an older stellar population by fitting an exponentially delayed plus burst star formation model increases the inferred stellar mass by 0.4 ± 0.2 dex. Since BEAGLE incorporates nebular line predictions from CLOUDY, photometric band contamination from strong optical lines is naturally and self-consistently modelled. We experiment with excluding the g and r bands (contaminated by the strong lines Hβ, [O III] 4959,5007, and Hα) and with including aperture-corrected *GALEX*

[3] http://www.jacopochevallard.org/beagle/

Table 4. Parameter estimates derived from broad-band SED fitting with BEAGLE (see Section 4 for details). These measurements indicate that the systems are low-mass (within the spectroscopic and photometric aperture: $\log_{10}(M/M_\odot) \sim 4.7$–$7.5$) and dominated by recent star formation, yielding extremely large specific star formation rates (median sSFR 100 Gyr^{-1} from photometry only). Note that the SFR indicated here is measured over the last 10 Myr.

SBID	$\log_{10}(M/M_\odot)$	$\log_{10}(SFR/(M_\odot\ yr^{-1}))$	$\hat{\tau}_V$
2	5.1 ± 0.0	−1.88 ± 0.04	0.57 ± 0.10
36	7.5 ± 0.2	−0.25 ± 0.08	0.08 ± 0.08
80	6.1 ± 0.1	−0.94 ± 0.06	0.33 ± 0.13
82	6.4 ± 0.1	−0.58 ± 0.06	0.25 ± 0.06
110	6.4 ± 0.1	−0.91 ± 0.05	0.02 ± 0.02
111	5.6 ± 0.2	−2.20 ± 0.10	0.19 ± 0.08
179	5.2 ± 0.1	−1.77 ± 0.05	0.20 ± 0.07
182	7.3 ± 0.1	0.23 ± 0.04	0.27 ± 0.05
191	4.9 ± 0.1	−2.11 ± 0.07	0.37 ± 0.07
198	4.7 ± 0.3	−2.27 ± 0.12	0.03 ± 0.04

magnitudes (using T-PHOT: Merlin et al. 2015), but neither has a significant effect on the derived masses or specific star formation rates. For simplicity and to avoid systematic error due to aperture effects, we present results from fitting the full set of SDSS photometry only (bands *u*, *g*, *r*, *i* and *z*) which probe the stellar continuum and strong optical emission lines from ∼3500 to 9000 Å. A visual inspection confirms that the *u*, *i* and *z* bands closely approximate the continuum in the SDSS spectra. The results are displayed in Table 4.

The photometric data suggest that the systems are dominated by recently formed stars. We infer total stellar masses spanning 2 orders of magnitude, from 10^5 to 10^7 $M_\odot$. The lowest-mass objects $\log_{10}M_\star/M_\odot \lesssim 5.5$ are predominantly giant H II regions embedded in nearby disc systems (SB 198, 191, 179; see Fig. 1). Adopting the *HST*/*COS* spectroscopic aperture as a rough measure of the size of the star-forming region probed, the implied stellar mass surface densities span approximately a half-dex around $10^{6.5}\ M_\odot/\ kpc^2$. They are generally unreddened, with *V*-band optical depth to dust $\hat{\tau}_V \lesssim 0.6$ (corresponding approximately to $A_V \lesssim 0.6$). The derived specific star formation rates (sSFRs) are uniformly high, 10–100 Gyr^{-1}, implying these systems have undergone intense recent star formation. These sSFRs are comparable to those measured for large samples of local extreme emission-line galaxies such as the green peas (Cardamone et al. 2009; Izotov, Guseva & Thuan 2011), though our objects are lower in mass than the median for such samples (∼$10^9\ M_\odot$ total with $10^7\ M_\odot$ in a recent burst; Izotov et al. 2011). The sSFRs in our sample are comparable to those inferred for photometric samples at $z \sim 7$ (Schaerer & de Barros 2010; Stark et al. 2013; Salmon et al. 2015), as well as those inferred from photoionization modelling of systems at z ∼6–7 with high-ionization UV line detections (Stark et al. 2015a; Stark 2016). Very young local star-forming galaxies such as these are likely to have moderately metal-poor gas and extreme nebular line emission reflecting the presence of numerous massive stars.

3.2 Gas conditions from optical spectra

Nebular lines in the optical spectra provide information about the ionization state, physical conditions and composition of the gas. We report diagnostic line ratios as well as several derived parameters in Tables 5 and 6. In these tables and in the rest of the paper (unless explicitly stated), all equivalent widths are measured in the rest frame. In these tables and in deriving quantities in this section, all line measurements are from SDSS with the exception of [O II] λ3727, which is measured in the MMT spectra where noted. For measurements involving [O II], we scale the MMT [O II] flux by the median ratio of strong lines measured in both SDSS and MMT for aperture correction. This correction factor varies by <10 per cent between lines spanning 3900–5000 Å for each object; we add an additional 10 per cent uncertainty in-quadrature to the measured [O II] λ3727 uncertainty to account for this aperture correction.

We use the direct-T_e method to measure gas-phase oxygen abundances. In particular, we determine the electron temperature and density appropriate for singly and doubly ionized oxygen separately using the `getCrossTemDen` method provided by `PyNeb` (Luridiana et al. 2015). For O II and O III, we fit a temperature-sensitive line ratio ([O II] λλ3726, 3729 / [O II] λλ7320, 7330 and [O III] λ4363 / [O III] λλ4959, 5007, respectively) alongside the density-sensitive [S II] λ6731 / [S II] λ6716 doublet. We adopt the most up-to-date atomic and collisional data packaged with `PyNeb` for the three species involved, since adjustments to these quantities can have a significant impact on the gas properties derived using forbidden-line diagnostics (e.g. Sanders et al. 2016). We use collision strengths from Tayal & Zatsarinny (2010) for [S II], Kisielius et al. (2009) for [O II], Storey, Sochi & Badnell (2014) for [O III] and atomic data from Fischer & Tachiev (2004) for [O II] and [O III] alongside Tayal & Zatsarinny (2010) for [S II]. With T_e and n_e measured directly for [O II] and [O III] in-hand, we then compute total gas-phase oxygen abundance from the [O II] λλ3726, 3729 and [O III] λλ4959, 5007 fluxes relative to H β using the `getIonAbundance` method in `PyNeb`. Uncertainties are propagated through this process by repeating the computation with resampled line fluxes from the line fit posterior distributions. As described in Section 2.7, we compute the intrinsic Case B Balmer spectrum used to estimate extinction with these T_e, n_e values, and iterate until convergence.

Table 5. Optical nebular line measurements (flux and equivalent width, uncorrected for extinction) and derived extinction (galactic and residual Balmer decrement).

SBID	H β (10^{-15} ergs s^{-1} cm^{-2})	H β W_0 (Å)	[O III] 4959, 5007 (10^{-15} ergs s^{-1} cm^{-2})	[O III] 4959,5007 W_0 (Å)	[O III] 4363 (10^{-15} ergs s^{-1} cm^{-2})	[N II] 6584 (10^{-15} ergs s^{-1} cm^{-2})	E(B-V) intrinsic (galactic)
2	67.4 ± 2.1	273 ± 16	516.6 ± 38.3	1844 ± 253	7.59 ± 0.12	2.68 ± 0.07	0.15 (0.05)
36	26.6 ± 0.4	93 ± 3	189.1 ± 6.0	592 ± 30	2.57 ± 0.10	1.64 ± 0.04	0.06 (0.02)
80	63.6 ± 2.4	243 ± 17	481.8 ± 26.2	1661 ± 173	3.30 ± 0.11	7.01 ± 0.21	0.13 (0.02)
82	54.7 ± 0.6	178 ± 4	496.5 ± 18.0	1304 ± 82	7.10 ± 0.14	3.09 ± 0.07	0.10 (0.03)
110	19.1 ± 0.3	86 ± 2	131.2 ± 3.4	542 ± 24	1.39 ± 0.06	2.19 ± 0.07	0.06 (0.01)
111	21.7 ± 0.6	102 ± 5	144.5 ± 6.5	642 ± 51	2.42 ± 0.11	0.65 ± 0.04	0.07 (0.02)
179	35.3 ± 0.7	196 ± 8	215.1 ± 9.5	1081 ± 92	1.15 ± 0.06	4.87 ± 0.17	0.17 (0.02)
182	33.6 ± 0.5	151 ± 4	276.4 ± 8.4	1053 ± 49	3.45 ± 0.08	2.26 ± 0.09	0.11 (0.02)
191	88.6 ± 3.2	393 ± 23	723.5 ± 59.8	2435 ± 306	4.04 ± 0.10	5.03 ± 0.14	0.02 (0.03)
198	32.3 ± 0.9	189 ± 11	167.9 ± 9.8	871 ± 96	1.06 ± 0.06	5.02 ± 0.24	0.10 (0.02)

Table 6. Optical nebular line ratios and derived gas physical conditions, all corrected for extinction. The O_{32} and R_{23} measurements come from both SDSS [1] and MMT [2].

SBID	O_{32}	R_{23}	[O III] 5007 / H β	[N II] 6584 / H α	n_e(S II) (cm^{-3})	T_e(O III) (10^4 K)	$12+\log_{10}$(O/H) direct-T_e	sSFR/Gyr^{-1} H α
2	$7.5^{+0.8}_{-0.6}$ [2]	$8.2^{+1.7}_{-1.1}$	5.59 ± 0.52	0.0113 ± 0.0005[a]	186^{+33}_{-32}	1.58 ± 0.05	7.81 ± 0.07	339^{+40a}_{-33}
36	$5.5^{+0.3}_{-0.3}$ [1]	$8.3^{+0.3}_{-0.3}$	5.27 ± 0.21	0.0200 ± 0.0008	119^{+37}_{-34}	1.49 ± 0.03	7.92 ± 0.04	19^{+10}_{-5}
80	$3.7^{+0.3}_{-0.3}$ [2]	$9.6^{+1.2}_{-1.1}$	5.58 ± 0.38	0.0324 ± 0.0027	168^{+44}_{-39}	1.15 ± 0.02	8.24 ± 0.06	187^{+33}_{-26}
82	$9.2^{+1.3}_{-1.1}$ [2]	$8.9^{+3.0}_{-1.8}$	6.73 ± 0.30	0.0174 ± 0.0010	158^{+47}_{-39}	1.54 ± 0.03	7.91 ± 0.04	177^{+53}_{-34}
110	$3.8^{+0.1}_{-0.1}$ [2]	$8.7^{+1.6}_{-1.2}$	5.10 ± 0.17	0.0377 ± 0.0020	70^{+36}_{-33}	1.33 ± 0.03	8.17 ± 0.08	37^{+9}_{-6}
111	$6.4^{+0.2}_{-0.2}$ [2]	$7.5^{+0.8}_{-0.5}$	4.92 ± 0.30	0.0097 ± 0.0007	22^{+26}_{-16}	1.65 ± 0.05	7.81 ± 0.08	21^{+13}_{-6}
179	$2.7^{+0.1}_{-0.1}$ [2]	$8.5^{+1.9}_{-1.4}$	4.43 ± 0.25	0.0389 ± 0.0034	117^{+34}_{-35}	1.07 ± 0.02	8.35 ± 0.07	214^{+74}_{-45}
182	$5.4^{+0.4}_{-0.3}$ [1]	$9.6^{+0.3}_{-0.3}$	6.08 ± 0.26	0.0208 ± 0.0014	125^{+37}_{-34}	1.45 ± 0.02	8.01 ± 0.04	91^{+22}_{-15}
191	$9.5^{+0.7}_{-0.9}$ [2]	$9.0^{+1.8}_{-1.5}$	6.07 ± 0.61	0.0187 ± 0.0033	95^{+81}_{-62}	1.05 ± 0.03	8.30 ± 0.07	128^{+35}_{-28}
198	$1.7^{+0.1}_{-0.2}$ [2]	$7.9^{+3.2}_{-1.6}$	3.81 ± 0.27	0.0475 ± 0.0051	42^{+29}_{-23}	1.11 ± 0.03	8.48 ± 0.11	146^{+281}_{-68}

Note. [a] Due to the complicated H α line profile for SB 2 (see Section 2.7), the dust-corrected H α flux is predicted by rescaling H β according to Case B.

In addition, we infer star formation rates from the H α luminosities by converting to an ionizing photon luminosity above 13.6 eV assuming Case B using the PyNeb-derived T_e and n_e, applying the ratio between ionizing photon luminosity and SFR derived from a $Z_\odot/5$ constant star formation history model at 100 Myr with a Chabrier (2003) IMF produced with BEAGLE (Chevallard & Charlot 2016). This is then compared to the stellar masses inferred from photometric SED fitting assuming the same IMF and a constant star formation history (see Table 4) to derive specific star formation rates. We present total oxygen abundances, T_e(O III), and n_e(S II), and specific star formation rates derived in this manner in Table 6.

The direct-T_e method as applied has the advantage of being independent from photoionization modelling and assumptions about the ionizing spectrum, but has some limitations. For simplicity, we ignore contributions from O^{3+} in this direct metallicity computation as we lack access to any lines from this species. Izotov et al. (2006) provide an approximate correction formula for this species based upon the He^{2+}/He^{+} ionic abundance; using the nebular He II λ4686 / He I λ6678 ratio measured in the high-resolution ESI data (dust-corrected, $\leq$2.2) and the abundance formulae provided by Benjamin, Skillman & Smits (1999), we find $He^{2+}/He^{+} \leq 0.06$, and a negligible $\lesssim$0.01 dex correction to our derived oxygen abundances. Recently, Paalvast & Brinchmann (2017) described a systematic offset towards lower T_e-derived metallicities at very low star formation rates due to stochastic IMF sampling, but they predict this effect to be negligible ($\ll$0.1 dex) at the star-formation rates probed here ($\gtrsim 10^{-2}$ M$_\odot$ yr^{-1}). Finally, this method implicitly assumes a simplified two-zone ionization structure, but note that the metallicities derived here are in reasonable agreement with those derived from full photoionization modelling of the strong UV and optical lines, as described in Section 3.3.

The optical line measurements confirm the extreme nature of these objects. The strengths of H α and [O III] are very different from typical nearby galaxies. The star formation rates inferred from H α validate the very large specific star formation rates suggested by the SED fits (Table 4), spanning the range 20–300 Gyr^{-1}. Our objects all have >500 Å equivalent width [O III] λλ4959, 5007 and $\gtrsim$100 Å H β emission, placing them securely in the realm of rare $z \sim 0$ extreme emission line galaxies (e.g. Cardamone et al. 2009; Izotov et al. 2011). While rare at low-redshift, optical equivalent widths of the magnitude observed here have been inferred routinely from *Spitzer* Infrared Array Camera (IRAC) band contamination in

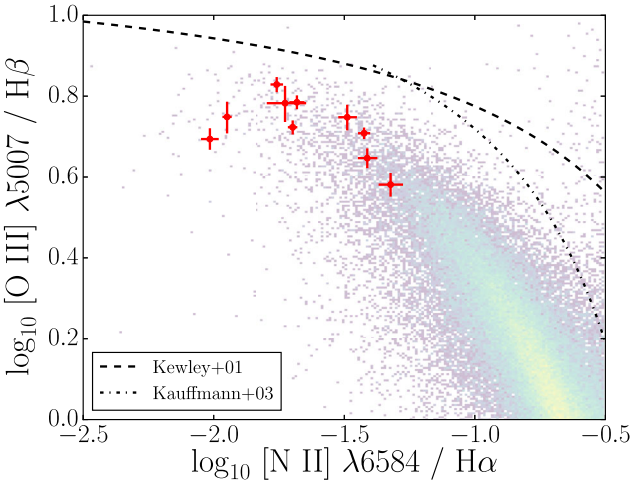

Figure 3. The relevant segment of the BPT diagram depicting our sources (red) and the log-histogram of SDSS galaxies with S/N > 3 in each of the relevant lines (background density plot). The maximum starburst lines of Kewley et al. (2001, theoretical) and Kauffmann et al. (2003, empirically modified) are displayed as dashed lines. Our galaxies lie in the extreme tail of the star-forming sequence, with very high [O III]/H β ratios.

systems at $z \gtrsim 7$ (e.g. Labbé et al. 2013; Smit et al. 2014; Huang et al. 2016; Roberts-Borsani et al. 2016). As for the photometric measurements above, this suggests that the relative intensity of star formation in these systems is comparable to that occurring in UV-selected galaxies at high redshift.

The gas in these systems is both metal-poor and highly ionized. The direct-temperature metallicities range from $12+\log_{10}$(O/H) ~7.8–8.5, i.e. $\sim Z_\odot/8 - Z_\odot/2$. In the BPT diagram (Fig. 3), they lie in the extreme tail of the star-forming sequence towards low [N II]/H α and high [O III]/H β. Our objects show no signs of a deviation from the local SDSS star-forming locus towards higher [N II]/H α as observed at $z \sim$ 2–3 (e.g. Steidel et al. 2014; Shapley et al. 2015; Sanders et al. 2016; Kashino et al. 2017; Strom et al. 2017); note that this is a natural consequence of their selection using BPT diagram cuts designed to select $z \sim 0$ star-forming galaxies (Shirazi & Brinchmann 2012). The quantity O_{32} = [O III] λ4959 + λ5007 / [O II] λλ3727, 3729, a proxy for the ionization parameter (or density of ionizing radiation), is also significantly larger than in typical star-forming galaxies nearby. The O_{32} ratio

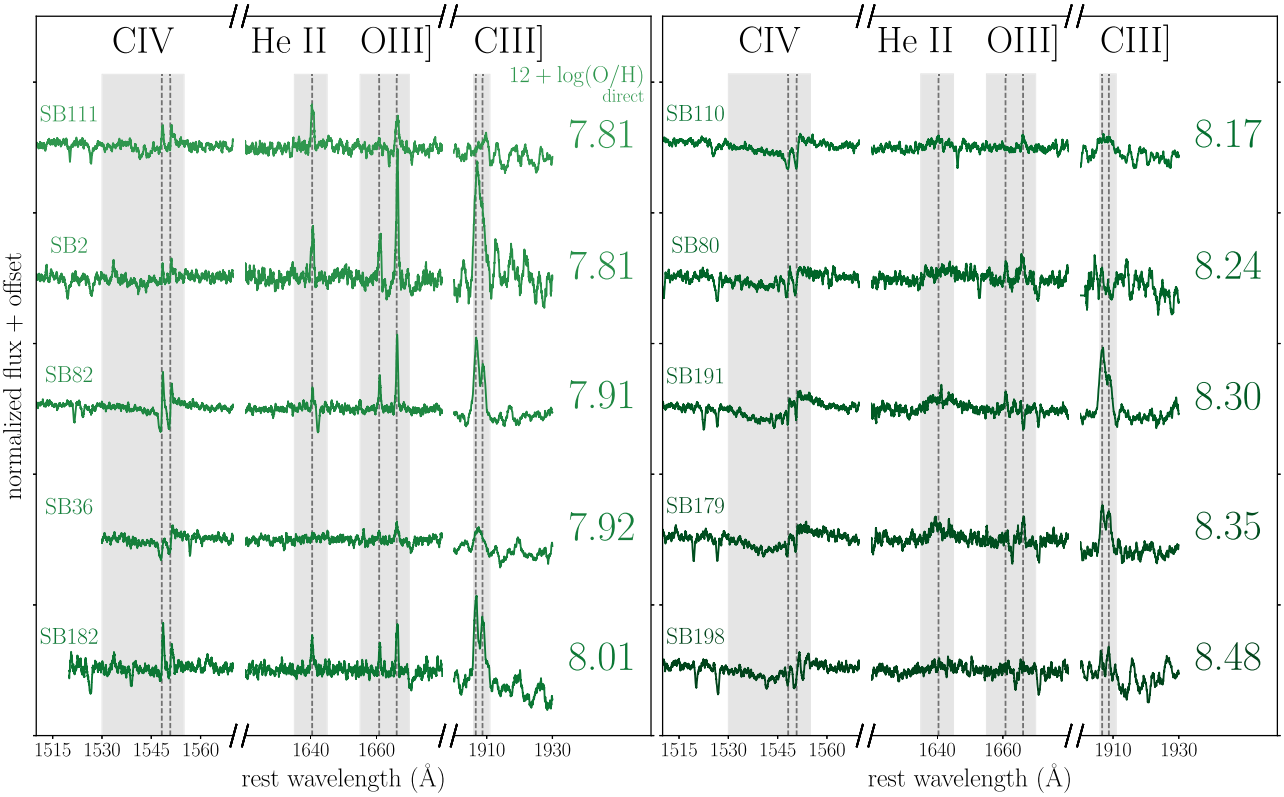

Figure 4. The *HST*/*COS* spectra obtained for our systems, ranked by gas-phase metallicity obtained via the direct method applied to the optical oxygen lines (see Section 3.2). The spectra have been median-normalized and offset vertically for display; and the key metal lines (C IV, He II, O III], C III]) are highlighted. The relatively metal-poor objects (left-hand panel, $12 + \log_{10}\mathrm{O/H} \lesssim 7.9$) show extreme emission in these lines, with the C III] doublet reaching equivalent widths ∼15 Å and nebular He II, C IV appearing in four of the five, emission rarely seen in typical star-forming galaxies. In contrast, above this metallicity the spectra show relatively weak nebular emission (except C III], which still reaches equivalent widths ∼10 Å in SB 179 and 191) and are increasingly dominated by stellar wind features in C IV and He II.

ranges from 2 to 10 in our sample with a median of 6, whereas the vast majority of nearby SDSS galaxies present $O_{32} \lesssim 1$ (e.g. Sanders et al. 2016) at similar R_{23} (=[O III] λ4959 + λ5007 + [O II] λλ3727, 3729 / H β). These extreme O_{32} values indicate that the gas in these objects is exposed to ionizing radiation from very recently formed stars, and may imply significant Lyman continuum escape (e.g. Jaskot & Oey 2013; Izotov et al. 2016; Stasińska et al. 2015).

The photometry and optical spectroscopy together reveal systems dominated by recent star formation (sSFR $\sim 100\,\mathrm{Gyr}^{-1}$) with little intrinsic dust reddening ($E(B-V) \lesssim 0.1$) and extreme optical line emission (O III] λλ4959, 5007 EWs ∼500–2500 Å). Systems with comparable properties observed in the rest-UV at $z \sim 2$ reveal strong UV nebular emission, with C III] emission reaching EWs of ∼15 Å (e.g. Erb et al. 2010; Stark et al. 2014); and at the highest redshifts, similarly strong C III] and even more extreme C IV at ∼40 Å (Stark et al. 2015a,b; Stark 2016; Mainali et al. 2017). Though strong UV nebular emission appears to be common at the highest redshifts, the stellar populations which power it and its dependence on bulk galaxy properties (metallicity, ionization parameter) remain unclear.

3.3 The UV spectra

The *HST*/*COS* FUV and NUV spectra reveal extreme nebular emission and strong stellar features from the winds of massive stars. Despite the fact that the systems are uniformly undergoing extreme star formation (sSFR $\gtrsim 20\,\mathrm{Gyr}^{-1}$), there is significant variation in their UV nebular properties. We plot the spectra in Fig. 4 with key features highlighted and present nebular line measurements in Tables 7 and 8.

Fig. 4 highlights a clear metallicity trend in the UV spectra. Above $12 + \log \mathrm{O/H} > 8.1$, the average object is characterized by prominent stellar wind features – deep C IV λλ1548, 1550 P-Cygni stellar wind features (dominated by massive O stars) and broad He II λ1640 emission (produced in the dense, highly ionized winds of WR stars and very massive OIf supergiants). The stellar winds of O stars are driven by metal line opacities and observed via a carbon transition, and are thus inherently metallicity-dependent. The winds of WR stars likely depend similarly on metallicity – we discuss these winds in more detail in Section 5.3. The most extreme nebular lines (He II, C IV) are undetected in this metal-rich subset. In contrast, the spectra of the more metal-poor objects ($12 + \log \mathrm{O/H} \lesssim 8.0$) show weak stellar C IV and He II features and are instead dominated by nebular emission in C III, C IV and He II.

We discuss the UV spectrum of each object in the context of their optical measurements individually below, in order of decreasing gas-phase direct-T_e metallicity.

The most metal-rich object in our sample (at $12 + \log \mathrm{O/H} = 8.48$, or $Z_\odot/2$) is **SB 198**, a star-forming region of stellar mass $10^{4.7}\,M_\odot$ embedded in a spiral galaxy at 16.5 Mpc. The UV spectrum of this object is dominated by the C IV P-Cygni feature. For this and all following objects, we quantify the strength of the C IV wind feature by integrating the absorption component over 1528–1551 Å, with continuum defined as a linear

Table 7. UV nebular emission line flux measurements for C IV, He II, O III], and C III] in the *HST*/*COS* UV spectra. We provide 3σ upper limits when possible. The O III] 1666 line in SB 191 is obscured by MW absorption.

SBID	C IV 1548 (10^{-15} ergs s^{-1} cm^{-2})	C IV 1550 (10^{-15} ergs s^{-1} cm^{-2})	He II 1640 (10^{-15} ergs s^{-1} cm^{-2})	O III] 1661 (10^{-15} ergs s^{-1} cm^{-2})	O III] 1666 (10^{-15} ergs s^{-1} cm^{-2})	C III] 1907, 1909 (10^{-15} ergs s^{-1} cm^{-2})
2	0.20 ± 0.02	0.19 ± 0.01	1.45 ± 0.06	1.40 ± 0.04	3.35 ± 0.04	11.06 ± 0.63
36	<3.3	<3.3	<1.1	0.70 ± 0.06	2.16 ± 0.08	7.60 ± 0.88
80	<1.6	<1.6	<0.8	0.60 ± 0.04	1.69 ± 0.07	<4.1
82	1.92 ± 0.05	1.32 ± 0.05	1.22 ± 0.05	2.33 ± 0.05	5.05 ± 0.05	22.05 ± 0.40
110	0.20 ± 0.05	1.14 ± 0.09	<1.2	<0.9	1.28 ± 0.05	<5.2
111	0.79 ± 0.04	0.49 ± 0.03	2.37 ± 0.05	0.56 ± 0.06	2.68 ± 0.07	<3.9
179	<2.0	<2.0	<0.8	<1.1	1.36 ± 0.06	6.80 ± 0.23
182	1.54 ± 0.04	0.94 ± 0.05	1.42 ± 0.05	0.99 ± 0.04	2.27 ± 0.05	12.30 ± 0.33
191	<1.0	<1.0	<1.0	1.19 ± 0.07	–	15.91 ± 0.39
198	<3.1	<3.1	<0.8	<1.1	<1.1	3.79 ± 0.30

Table 8. Equivalent widths of the UV nebular emission lines. We provide 3σ upper limits when possible. The O III] 1666 line in SB 191 is wiped out by MW absorption.

SBID	C IV 1548 (Å)	C IV 1550 (Å)	He II 1640 (Å)	O III] 1661 (Å)	O III] 1666 (Å)	C III] 1907, 1909 (Å)
2	0.25 ± 0.02	0.22 ± 0.02	1.70 ± 0.06	1.94 ± 0.06	5.05 ± 0.10	14.86 ± 1.07
36	<0.4	<0.4	<0.4	0.26 ± 0.02	0.84 ± 0.03	4.98 ± 0.59
80	<0.5	<0.4	<0.7	0.55 ± 0.04	1.68 ± 0.08	<4.0
82	0.67 ± 0.02	0.41 ± 0.02	0.44 ± 0.02	0.85 ± 0.02	1.89 ± 0.02	12.09 ± 0.30
110	0.08 ± 0.02	0.37 ± 0.03	<0.4	<0.3	0.48 ± 0.02	<2.8
111	0.41 ± 0.02	0.24 ± 0.01	1.42 ± 0.03	0.35 ± 0.04	1.73 ± 0.05	<3.3
179	<0.5	<0.4	<0.6	<0.9	1.17 ± 0.06	8.71 ± 0.42
182	0.96 ± 0.03	0.55 ± 0.03	0.94 ± 0.04	0.70 ± 0.03	1.73 ± 0.04	13.35 ± 0.52
191	<0.5	<0.4	<0.5	0.64 ± 0.04	–	11.33 ± 0.34
198	<0.7	<0.6	<0.5	<0.8	<0.9	3.38 ± 0.31

fit to flux on either side of this interval. Before integrating this feature, we subtract Gaussian fits to any nebular ($\sigma < 200$ km s^{-1}) C IV emission and absorption present with continuum defined as a local linear model, and smooth via Fourier filtering to resolution >200 km s^{-1} to remove residual MW absorption features. This results in a C IV absorption equivalent width of -5.2 ± 0.2 Å. The C III] doublet is detected at 3 Å EW, but the O III] lines are not. Despite an extremely large sSFR of 150 Gyr^{-1}, the system shows a very low O_{32} of 1.7 and comparatively minimal UV nebular emission.

The next most metal-rich object is **SB 179** at $12 + \log \mathrm{O/H} = 8.35$. This is another giant H II region/super star cluster complex embedded in a larger disc system at 25 Mpc, with a correspondingly low mass ($10^{5.2}$ M$_\odot$). The UV spectrum reveals a prominent C IV P-Cygni stellar feature and clear nebular emission from C III] and O III]. The C IV absorption equivalent width is measured at -5.6, comparable to that of SB 198. However, SB 179 shows prominent broad stellar He II emission as well, as expected given the detection of broad wind emission in the optical SDSS spectra (see Table 1 and Shirazi & Brinchmann 2012). This wind emission is indicative of a substantial population of WR stars, which we discuss in more detail in Section 3.4. A two-component fit to He II λ1640 identifies purely broad 1600 km s^{-1} FWHM emission with equivalent width $3.1^{+0.3}_{-0.7}$ Å. Strong C III] is detected in this system at 8.7 Å equivalent width.

The next most metal-rich object in our sample (at $12 + \log \mathrm{O/H} = 8.30$) is **SB 191**, a $10^{4.9}$ M$_\odot$ star-forming region in a barred-spiral at 10 Mpc. SB 191 is marked by very prominent stellar C IV and He II features in the FUV, similar to SB 179. The C IV stellar absorption in the spectrum of SB 191 has EW -6.7 ± 0.1 Å, and the He II stellar emission fit yields equivalent width 4.3 ± 0.4 Å – one of the largest values attained in nearby star-forming regions (cf. Wofford et al. 2014; Smith et al. 2016). Nebular O III] λ1661 is detected at equivalent width 0.7 Å, but the 1666 component of the doublet is contaminated by an Al II MW absorption line. The C III] doublet is very prominent, with an equivalent width of 11 Å. Neither nebular He II nor C IV is detected to a 3σ upper limits of 0.5 Å. This object has the largest H β equivalent width in our sample at 400 Å (sSFR of 130 Gyr^{-1}), and an extremely large O_{32} of 10, further confirming that this object is undergoing a rapid buildup of massive stars.

SB 80 at $12 + \log \mathrm{O/H} = 8.24$ is another embedded H II region, this time at 46 Mpc with stellar mass $10^{6.1}$ M$_\odot$. The UV spectrum shows clear stellar He II (3.1 ± 0.3) and stellar C IV absorption (-4.3 ± 0.2). The only nebular lines detected are the O III] doublet at 2.2 Å combined EW (with a 3σ upper limit to C III] < 4 Å). The O_{32} ratio of this system is quite low relative to the rest of the sample at 3.7, implying a relatively low ionization parameter.

SB 110 is an isolated compact system (63 Mpc, $10^{6.4}$ M$_\odot$) at $12 + \log \mathrm{O/H} = 8.17$. Stellar He II emission is visible, though significantly less obvious than in SB 191 and 179. The C IV P-Cygni absorption has about the same depth as SB 80, at -4.4 Å. The C III] doublet is undetected at $\lesssim 3\sigma$ (<3 Å), making O III] 1666 the only confidently measured nebular line at EW 0.5 Å.

The next system, **SB 182**, presents a substantially different UV spectrum. This object is at gas-phase metallicity $12 + \log \mathrm{O/H} = 8.01$, or $Z/Z_\odot \simeq 1/5$. It is an isolated compact galaxy with the second-highest mass ($10^{7.3}$ M$_\odot$) of the sample. At a distance of 191 Mpc, the *HST*/*COS* aperture radius subtends the

largest physical scale probed by our UV spectra: ∼1.2 kpc. The UV stellar features have nearly disappeared (stellar C IV absorption EW >-1.5 Å and no clear stellar He II), and the *HST*/*COS* spectra are instead characterized by intense nebular emission. The C III] doublet reaches 13 Å and O III] λ1666 nearly 2 Å. In addition to C III] and O III] emission, we now see nebular He II (at EW 0.95 Å) and nebular C IV (doublet combined EW 1.5 Å). The presence of nebular He II emission (requiring substantial flux <228 Å) and the large ratio $O_{32} = 5.4$ suggest both a large ionization parameter and a hard ionizing spectrum.

SB 36 ($12 + \log O/H = 7.92$) is another isolated system (141 Mpc away) with similar stellar mass ($10^{7.5}$ $M_\odot$) to SB 182. Its lower H β EW (93 Å compared to 150 Å in SB 182, the second-lowest in the sample) presages its weaker UV nebular spectrum. Both C III] (EW ∼ 5 Å) and O III are detected, but nebular C IV and He II are not (<0.4 Å EW).

SB 82 ($12 + \log O/H = 7.91$), a compact galaxy with $10^{6.4}$ $M_\odot$ in stars at 76 Mpc, shows extreme UV emission. Though there is some hint of a C IV P-Cygni feature (equivalent width of absorption 1.5 ± 0.1 Å), C IV nebular emission is clearly present (at combined EW 1.1 Å). We also detect nebular He II λ1640 at EW 0.5 Å (the nearby MW absorption line does not impact this measurement; we fit it simultaneously with the nebular emission). The C III] doublet is measured at 12 Å EW. The extreme O_{32} ratio of 9 measured for this system is similar to the relatively metal-rich object SB 191, but here both nebular C IV and He II are confidently detected alongside the strong C III] emission.

The first of the two most metal-poor systems, **SB 2** ($12 + \log O/H = 7.81$, $\sim Z_\odot/8$), is comparable to SB 82 and 182 in its UV spectrum. This BCD component is closer (19 Mpc) and lower in mass ($10^{5.1}$ $M_\odot$) than SB 82 and 182 and presents very strong H β (EW of 270 Å) and large $O_{32} = 7.5$. The C III] EW achieved is the highest in this sample, at nearly 15 Å. Both nebular He II and C IV are detected, with He II at 1.7 Å and C IV at 0.5 Å combined EW.

Finally, **SB 111** is a low-mass ($10^{5.6}$ $M_\odot$) compact galaxy 16 Mpc away and also at gas-phase metallicity $12 + \log O/H = 7.81$. The UV spectrum shows nebular He II (1.4 Å) and C IV (combined 0.65 Å), as well as O III] (with a strong 1666 component at 2.7 Å); yet C III] is undetected (<4 Å EW). The detection of both C IV and He II suggests that SB 111 has significant hard ionizing flux beyond ∼50 eV.

Before discussing fits to the full UV spectra (Section 4), we examine the measured nebular emission in C IV, C III], and O III] in the context of photoionization modelling. These lines provide a nearly direct estimate of the relative abundance of carbon in the ISM (e.g. Garnett et al. 1995), and together with the strong optical lines paint a clearer picture of the state of ionized gas in these objects. We compare the measured fluxes of nebular C IV λλ1548, 1551, O III] λλ1661, 1666, and C III] λλ1907, 1909 along with [O III] λλ4959, 5007, [O III] λ4363, [O II] λ3727, H α, and H β to the grid of models described by Gutkin et al. (2016). The main adjustable parameters of this model are described in Gutkin et al. (2016) and Section 4 below; in particular, here we allow C/O, the density of the photoionized ISM n_H, the upper-mass cut-off of the IMF m_{up}, and the typical ionization parameter of newly formed H II regions U_S to vary. We adopt a simplified version of the attenuation model described by Charlot & Fall (2000) in this analysis, assuming a slope $\lambda^{-1.3}$ in birth clouds and $\lambda^{-0.7}$ in the ambient ISM. For simplicity, we adopt a constant star formation model fixed at an age of 100 Myr. We derive parameter estimates and 68 per cent confidence intervals for U_S, C/O and $\hat{\tau}_V$ using a χ^2 analysis; the results are displayed in Table 9. These strong emission lines are very well-fit by this model, and prefer gas-phase metallicities and attenuation optical depths in good agreement with those measured above, with median offset from the direct-T_e measurements of 0.2 ± 0.4 dex. In addition, this modelling suggests that the gas in these systems is highly ionized ($-4 < \log U_S < -2$) and subsolar in carbon abundance ($-1.4 \lesssim \log(C/O) \lesssim -0.5$). Note that while this method of deriving C/O differs from the T_e method applied by Berg et al. (2016), it is similar to the method of Pérez-Montero & Amorín (2017, found to be consistent with T_e) and the bulk range of derived abundances is consistent with that found for galaxies of similar metallicity using these methods. We discuss implications of the derived C/O measurements in more detail in Section 5.1 below.

Table 9. Parameter estimates derived from comparison of strong optical and nebular C IV, O III], and C III] UV emission line fluxes to the Gutkin et al. (2016) stellar photoionization model grid.

SBID	$\log U_S$	$\log(C/O)$	$\hat{\tau}_V$
2	$-4.00^{+0.25}_{-0.25}$	$-1.36^{+0.06}_{-0.06}$	$0.00^{+0.05}$
36	$-2.75^{+0.17}_{-0.17}$	$-0.81^{+0.09}_{-0.24}$	$0.19^{+0.11}_{-0.06}$
80	$-2.75^{+0.17}_{-0.17}$	$-0.74^{+0.35}_{-0.54}$	$0.26^{+0.26}_{-0.12}$
82	$-2.25^{+0.17}_{-0.17}$	$-0.52^{+0.04}_{-0.04}$	$0.53^{+0.04}_{-0.18}$
110	$-2.75^{+0.17}_{-0.17}$	$-0.68^{+0.17}_{-0.38}$	$0.07^{+0.08}_{-0.05}$
111	$-2.74^{+0.18}_{-0.18}$	$-1.02^{+0.23}_{-0.07}$	$0.12^{+0.11}_{-0.08}$
179	$-3.25^{+0.17}_{-0.17}$	$-1.01^{+0.23}_{-0.07}$	$0.05^{+0.03}_{-0.03}$
182	$-2.75^{+0.17}_{-0.17}$	$-0.75^{+0.10}_{-0.07}$	$0.22^{+0.05}_{-0.08}$
191	$-2.25^{+0.17}_{-0.17}$	$-0.74^{+0.10}_{-0.07}$	$0.00^{+0.09}$
198	$-3.25^{+0.17}_{-0.17}$	$-0.80^{+0.13}_{-0.25}$	$0.13^{+0.17}_{-0.12}$

3.4 The ESI spectra

As hot massive stars, WR stars may be an important source of the ionizing radiation necessary to power the observed UV nebular emission. The *HST*/*COS* spectra reveal strong stellar He II λ1640 emission in several systems (Fig. 4). In particular, three objects above $12 + \log O/H > 8.2$ have broad 1600 km s^{-1} FWHM He II components with equivalent widths >2 Å (SB 80, 191, 179). To further characterize the WR populations present and ultimately assess their impact on the UV spectra, we also investigate WR emission in the deep optical ESI data.

WR stars are O stars stripped of their outer layers of hydrogen and observationally defined by the presence of broad emission lines from highly ionized winds (e.g. Crowther 2007). This includes lines of helium and nitrogen (CNO cycle) as well as carbon and sometimes oxygen (triple-α process) – nuclear-processed material being swept off the exposed core of a massive star. The WR class is subdivided primarily into two categories. WN stars are dominated by lines of helium and nitrogen from hydrogen burning, especially He II 1640, 4696. In contrast, WC stars primarily show carbon emission, particularly C IV λ5808. The relative numbers of these subtypes can inform an understanding of how these stars are produced – likely some combination of wind-driven mass loss and binary mass transfer at low metallicity (e.g. Conti 1976; Maeder & Meynet 1994; Schaerer & Vacca 1998; Eldridge & Stanway 2009). Very massive OIf supergiants can also contribute to broad He II emission during their hydrogen-burning main sequence lifetime, as they drive similar dense ionized winds during this time (e.g. Crowther et al. 2016; Smith et al. 2016).

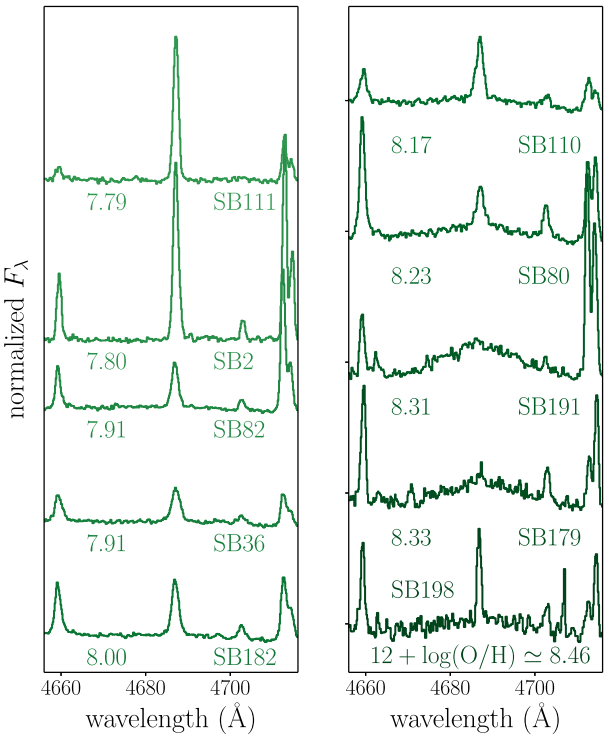

Figure 5. Cutouts of Keck/ESI optical spectra centred on the He II λ4686 line for all 10 objects, ordered by gas-phase direct-T_e metallicity. The more metal-poor galaxies in our sample tend to show stronger nebular emission and weaker broad stellar components, which suggests evolution in both the stellar winds and ionizing spectral slope with metallicity.

The impact of WR and WR-like stars on high-ionization emission remains unclear. The Lyman continuum flux from WR stars is generally comparable to that of O stars, but the contribution to He^+-ionizing flux may be substantial for the hottest WR stars (Crowther 2007). Stellar population synthesis models often predict a boost in photons beyond <228 Å in the short timespan when WR stars are active (e.g. Schaerer & Vacca 1998; Leitherer et al. 1999; Vidal-García et al. 2017), suggesting that they may play a large role in powering high-ionization nebular emission. However, previous observational studies have found nebular He II emission without accompanying WR signatures (e.g. Garnett et al. 1991; Brinchmann et al. 2008b; Shirazi & Brinchmann 2012). Determining the impact these stars have on UV nebular emission is critical for interpreting UV lines at high redshift.

The resolution of the ESI data allows us to confidently identify broad FWHM >150 km s^{-1} emission in the He II λ4686 Å line. We plot the ESI spectra centred on this line in Fig. 5. The results of a simultaneous fit to the broad and narrow components to the lines are displayed in Table 10; since the region around this transition is crowded with other nebular lines, we use median-filtering (with kernel size 10 Å) to better represent the continuum beyond 25 Å from line centre. As seen for He II λ1640 with *HST*/*COS* (Section 3.3), the ESI data reveal a range of He II λ4686 nebular strengths; from undetected to He IIλ4686/H$\beta \simeq 4 \times 10^{-3}$. Two systems (SB 179 and 191) reveal purely stellar He II emission, mistaken in low-resolution SDSS spectra for nebular. Broad components are detected only in the five most metal-rich systems, above $12 + \log O/H > 8.1$ ($Z/Z_\odot > 1/4$). These are uniformly measured at 1200 km s^{-1} FWHM, with fluxes relative to H$\beta \sim 10^{-2}$ (Table 10). We also investigate the dominant line emitted by WC stars, C IV λ5808 Å. This line is detected at $\gtrsim 3\sigma$ in four galaxies (80, 110, 179 and 191) with 5–15 per cent the stellar He II λ4686 flux.

Table 10. He II stellar and nebular fluxes measured from simultaneous two-component fits to the ESI data. The WR-to-O star ratio is estimated as described in Section 3.4. Upper limits represent the 84th-percentile confidence interval.

SBID	He II λ4686 / Hβ nebular ($\times 10^3$)	He II λ4686 / Hβ stellar ($\times 10^3$)	N(WR)/N(O)
2	13.0 ± 0.6	<3.4	<0.02
36	14.6 ± 0.5	<13.3	<0.06
80	3.1 ± 0.3	12.0 ± 0.9	0.05
82	8.5 ± 0.2	<6.4	<0.03
110	15.3 ± 0.5	22.6 ± 1.6	0.09
111	39.4 ± 1.3	<5.9	<0.03
179	<1.4	14.8 ± 1.1	0.05
182	12.4 ± 0.6	<4.6	<0.02
191	<1.4	13.5 ± 1.2	0.05
198	4.3 ± 0.3	12.0 ± 1.2	0.04

We can also constrain the number of WR stars relative to O stars present in these systems. This measurement comes with a significant caveat: since WR winds are metallicity-dependent (discussed further in Section 5.3), we must use a scaling relation to estimate the wind line luminosity of WN and WC stars at the gas-phase metallicity of each galaxy. The resulting number estimates are subject directly to systematic uncertainties in these wind scalings, which are presently calibrated with individual SMC and LMC stars (Crowther & Hadfield 2006). For simplicity, we assume that only WN stars are present – the flux of the C IV λ5808 stellar feature (using the wind luminosity scalings below) implies very small WCE/WNL ratios <10 per cent. This is consistent with expectations from population synthesis models (e.g. Eldridge & Vink 2006) that at these metallicities stripping is insufficient to reach He-burning products.[4] In this simple calculation we do not correct for OIf supergiants, as we are primarily interested in the relative number of massive stars driving dense ionized winds. Using the simple linear metallicity relation derived by López-Sánchez & Esteban (2010) from the models of Crowther & Hadfield (2006) to predict the line luminosity of a single WNL star, we estimate the ratio of WNL stars to the equivalent number of O7V stars derived from Hβ. For the five galaxies in which the stellar 4686 line is detected in our ESI spectra, we obtain a ratio of WR/O $\simeq 0.04 - 0.1$ (see Table 10). The remaining systems, at metallicities below $12 + \log O/H < 8.1$, appear to harbor smaller proportions of WR stars, $\lesssim 0.05$. These results are broadly consistent with that derived for larger samples of WR galaxies and with the predictions of binary population synthesis models (e.g. Brinchmann et al. 2008b; López-Sánchez & Esteban 2010).

4 FULL UV SPECTRAL SYNTHESIS

Stellar population synthesis coupled with photoionization modelling has become a commonplace tool in the analysis of galaxy spectra. However, comprehensive tests of this mode of analysis with typical data sets are difficult. In particular, while much work has been done to quantify the performance of different population

[4] However, it is important to note that SDSS samples will likely be biased against purely WC-dominated systems as the dichroic split occurs at 5900–6100 Å, near C IV λ5808 for low redshift galaxies.

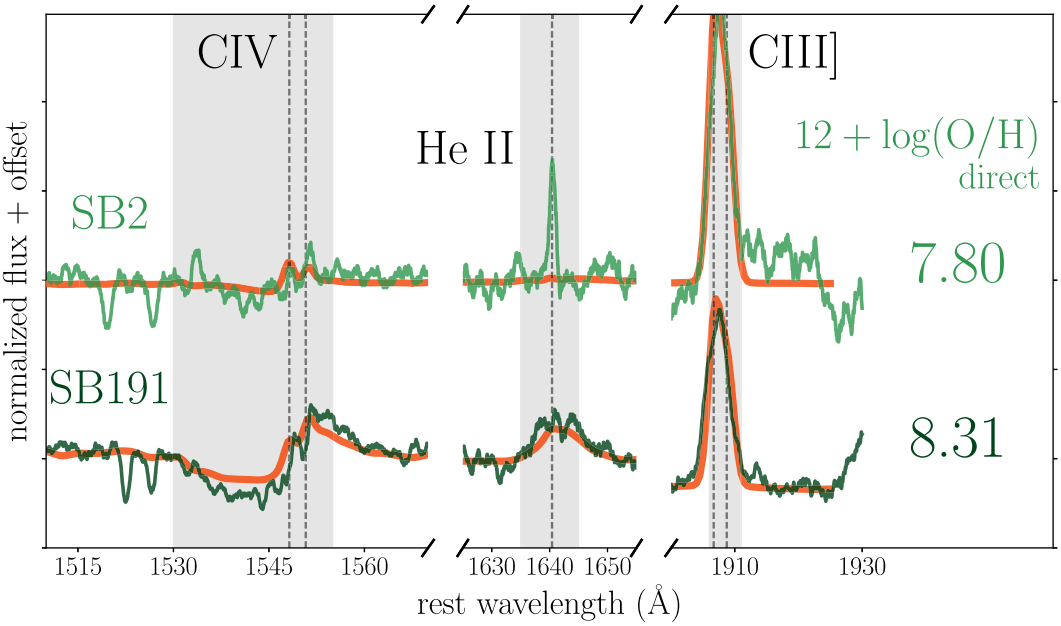

Figure 6. BEAGLE fits to the *HST*/*COS* UV spectra of two representative galaxies from our sample. The observed UV spectra are displayed in shades of green, and the maximum a posteriori estimation model is displayed as a thicker orange line (note that ISM/MW absorption lines were removed and the data were smoothed before fitting). The models are able to simultaneously reproduce well both stellar and nebular features in both cases, with the exception of nebular He II λ1640. The extremely strong stellar He II in SB 191 (and SB 179) is matched very well. However, the prominent nebular He II in SB 2 (and SB 111, 182) is not reproduced by the fiducial models without invoking extremely low metallicities inconsistent with the optical spectra.

synthesis models on photometric data (e.g. Wofford et al. 2014) and on integrated-light spectra probing older stellar populations (e.g. Bruzual & Charlot 2003; Schiavon, Caldwell & Rose 2004; Conroy, Gunn & White 2009), tests in the regime of young stellar populations dominated by massive stars and nebular emission are comparatively few. Recently, a joint analysis of optical and UV stellar and nebular features at $z \sim 2$ has become possible (Steidel et al. 2016), revealing significant discrepancies between inferred stellar and nebular abundances, but at these distances, this analysis can only be performed on stacked spectra or a small number of lensed systems. The data presented here provide a rare opportunity to test these tools and the underlying stellar models by fitting jointly both nebular emission and the wind features of the massive stars present in individual galaxies, covering a range of metallicities and UV spectral properties.

Here we present our initial results obtained by fitting the *COS* spectra of the 10 galaxies in our sample, while more extensive modelling results of these data will be presented in a companion paper (Chevallard et al., in preparation). We fit, pixel by pixel, the full *HST*/*COS* UV spectrum of each object, with the goal of matching both strong stellar and nebular features simultaneously. To achieve this, we use the Bayesian spectral interpretation tool BEAGLE (Chevallard & Charlot 2016), which incorporates in a flexible and consistent way the production of radiation in galaxies and its transfer through the interstellar and intergalactic media. Before running the fitting, we remove ISM and MW absorption features and smooth the spectra to a uniform resolution of 2.3 Å FWHM, appropriate for comparison to the stellar templates. We rely on the full set of models of Gutkin et al. (2016) which combine the latest version of the Bruzual & Charlot (2003) stellar population synthesis model with the standard photoionization code CLOUDY (Ferland et al. 2013) to compute the emission from stars and the interstellar gas. In particular, the nebular emission is computed following the prescription of Charlot & Longhetti 2001, where the main adjustable parameters of the photoionized gas are the interstellar metallicity, $Z_{\rm ISM}$, the dust-to-metal mass ratio, $\xi_{\rm d}$ (which characterizes the depletion of metals on to dust grains), and the typical ionization parameter of newly ionized H II regions, $U_{\rm S}$ (which characterizes the ratio of ionizing-photon to gas densities at the edge of the Stroemgren sphere). We consider here models with hydrogen density $n_{\rm H} = 100\,{\rm cm}^{-3}$ and C/O abundance ratios ranging from 0.1 to 1.0 times the solar ratio [$({\rm C/O})_{\odot} \approx 0.44$]. Finally, we describe attenuation by dust using the 2-component model of Charlot & Fall (2000).

Following Section 3.3, we adopt a constant star formation history of variable age, where we let the age freely vary in the range $6.0 \leq \log({\rm age yr}^{-1}) \leq 9$, finding negligible differences in the results when adopting a more complex SFH. We adopt a standard Chabrier (2003) initial mass function and we test two different values for the upper mass cut-off, 100 and 300 $M_{\odot}$. We further adopt the same metallicity for stars and star-forming gas ($Z = Z_{\rm ISM}$) and assume that all stars in a galaxy have the same metallicity, in the range $-2.2 \leq \log(Z/Z_{\odot}) \leq 0.25$. We let freely vary the dust-to-metal mass ratio and the ionization parameter in the ranges $0.1 \leq \xi_{\rm d} \leq 0.5$ and $-4 \leq \log U_{\rm S} \leq -1$, respectively. We consider V-band dust attenuation optical depths in the range $0 \leq \hat{\tau}_V \leq 5$ and let the fraction of this arising from dust in the diffuse ISM rather than in giant molecular clouds freely vary in the range $0 \leq \mu \leq 1$.

In Fig. 6 we show an example of a fit to a relatively metal-rich galaxy (SB 191; direct-T_e $12 + \log {\rm O/H} = 8.3$) and one of the most metal-poor systems (SB 2; direct-T_e $12 + \log {\rm O/H} = 7.8$). The stellar C IV and He II and nebular C III], O III], and C IV are reproduced very well in all cases while the prominent nebular He II emission in SB 2, 182 and 111 is difficult to achieve. Increasing the maximum allowed stellar mass $M_{\rm up}$ to 300 $M_{\odot}$ increases the strength of nebular He II, and does allow the emission in SB 111 to be fit, but only for extremely low metallicity $12 + \log {\rm O/H} \simeq 6.5$ inconsistent with the optical data. These fits will be explored in

quantitative detail in Chevallard et al., in preparation). We discuss the discrepant nebular He II empirically below.

5 DISCUSSION

Spectroscopy of local star-forming galaxies in the UV provides an important empirical baseline for interpreting observations at high redshift and informs our understanding of low-metallicity stellar populations. Deep observations at both $z \sim 2$ and now $z \sim 6$–7 have revealed emission in C III] and C IV far stronger than in typical star-forming systems at low redshift. The gas properties and stellar populations necessary and sufficient to power such high-ionization emission remain unclear, especially with limited existing data below $Z_{\odot}/3$. In Section 5.1 we discuss the empirical properties of the strong UV line emitters and the potential utility of UV nebular emission as diagnostics of physical conditions in the reionization era. Then we discuss the shape of the ionizing spectrum inferred from the nebular emission in Section 5.2, before addressing directly the possible sources of the necessary flux in Section 5.3.

5.1 Characterizing strong UV line emitters

Detections of strong C III], C IV and other high-ionization lines in the reionization era represent a new opportunity. Since they originate from species with ionization potentials in the range of extreme-UV photons, they are more sensitive to the most extreme radiation emitted by young metal-poor stellar populations. This sensitivity also makes these lines challenging to interpret – without an observational baseline, the results of photoionization modelling will be subject to substantial systematic uncertainties. To draw robust inferences about reionization-era galaxies from rest-UV nebular emission, we must develop an empirical understanding of the stellar populations and gas conditions which support these lines. This in turn requires a local sample of extreme UV line emitters to which photoionization modelling and high-redshift observations can be compared.

Nearby star-forming galaxies with high-ionization UV emission comparable to that seen at $z > 6$ have proved mostly elusive. Archival studies focused on selecting UV-bright star-forming galaxies have not yet identified a significant population analogous to that observed at $z \sim 7$. Individual galaxies at $z \sim 6$–7 have revealed C III] at rest-frame equivalent widths in excess of 20 Å (Stark et al. 2015a, 2017) and C IV at ∼20–40 Å (Stark et al. 2015b; Mainali et al. 2017). Only seven (one) star-forming galaxies with secure C III] equivalent widths >10 Å (>15 Å, respectively) have been found by *FOS*, *GHRS*, *IUE* and *COS*; and only three with detections of nebular C IV.[5]

The 10 star-forming galaxies presented here include four new extreme >10 Å C III] emitters, including the second highest C III] equivalent width detected locally at 15 Å (SB 2). In addition, our data constrain both stellar and nebular C IV and He II. Four of our UV spectra reveal clear nebular C IV and He II in emission, which (together with three strong emitters from the sample presented by Berg et al. 2016) allows us to conduct the first thorough analysis of these extreme UV lines in nearby star-forming galaxies. The detection rate of UV nebular emission in this sample selected to show He II emission in the optical is extremely high, with O III] detected in all but one; yet even in this sample we see a wide range of UV nebular properties.

[5] As discussed in Appendix B, this ignores two star-forming regions in the LMC and SMC for which the *FOS* aperture subtends a very small physical distance, and Tol 1214-277, where the continuum was undetected by *FOS*.

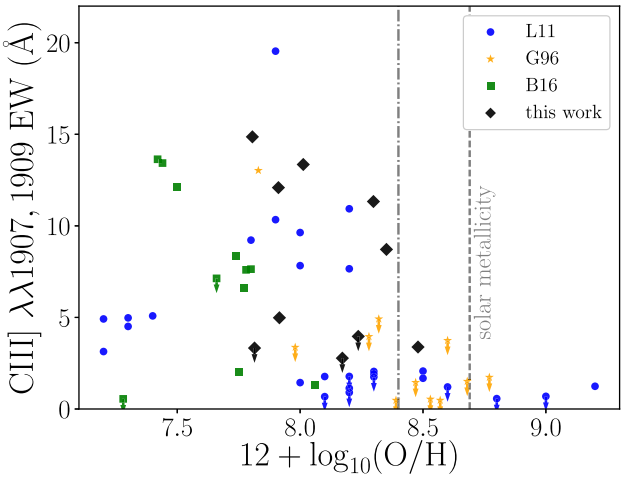

Figure 7. Equivalent width of the combined C III] λλ1907, 1909 semiforbidden doublet as a function of gas-phase metallicity. In addition to the *HST*/*COS* data presented in this paper, we plot archival data from nearby galaxies catalogued by Leitherer et al. (2011, L11), Giavalisco et al. (1996, G96) and Berg et al. (2016, B16) – see Appendix B for more details. These data suggest an empirical metallicity threshold for C III]: above 12 + log O/H ∼ 8.4 (marked by the dash-dotted line), C III] equivalent widths do not exceed ∼5 Å. Below this threshold, extremely high equivalent widths ≳15 Å are achieved (comparable to that observed in the reionization era: Stark et al. 2015a, 2017), though not uniformly.

We expect metallicity to play a role in modulating UV nebular emission. Metal-poor gas cools less efficiently, leading to higher electron temperatures and stronger collisionally excited emission, and lower metallicity stars evolve to hotter effective temperatures with weaker winds, yielding harder emergent stellar spectra (e.g. Schaller et al. 1992; Schaerer 2003). Previous authors have found unclear trends between C III] equivalent width and metallicity, focusing on the large scatter at fixed metallicity (e.g. Bayliss et al. 2014; Rigby et al. 2015). In Fig. 7, we plot the C III] doublet equivalent widths versus gas-phase metallicity for our sample as well as for archival local data gathered from *IUE*, *GHRS*, *FOS* and *COS* (see Appendix B). There is a striking transition with metallicity evident in these local galaxies. Above 12 + log O/H ≳ 8.4, C III] equivalent widths do not exceed ∼5 Å, and only reach a median of 0.9 Å. Below this metallicity ($Z/Z_{\odot} \lesssim 1/2$), the median increases by a factor of 5 (to 5.0 Å), and individual systems display extremely strong emission ∼15–20 Å, approaching reionization-era values. In our sample, we see a hint of evolution below half-solar metallicity as well, with stronger median equivalent width at and below metallicities 12 + log O/H ≲ 8.0 (∼12 Å) than above (∼3.4 Å). We observe a similar trend in O III] λλ1661, 1666 in our sample, with galaxies below $Z/Z_{\odot} \lesssim 1/5$ reaching median doublet equivalent width 2.4 Å, three times higher than at higher metallicities (0.8 Å). Evidently, metallicity has a substantial effect on UV nebular emission; suppressing strong C III] and O III] entirely above a half-solar, and enhancing it at yet lower metallicities (at least down to $Z/Z_{\odot} \sim 1/8$).

Our data reveal a similar but lower threshold for nebular C IV and He II production. As is clear in Fig. 4, we detect nebular C IV and He II in four of the five most metal-poor objects, but none above 12 + log O/H > 8.0 ($Z/Z_{\odot} > 1/5$). The three detections of likely nebular C IV and He II from Berg et al. (2016) all occur in systems

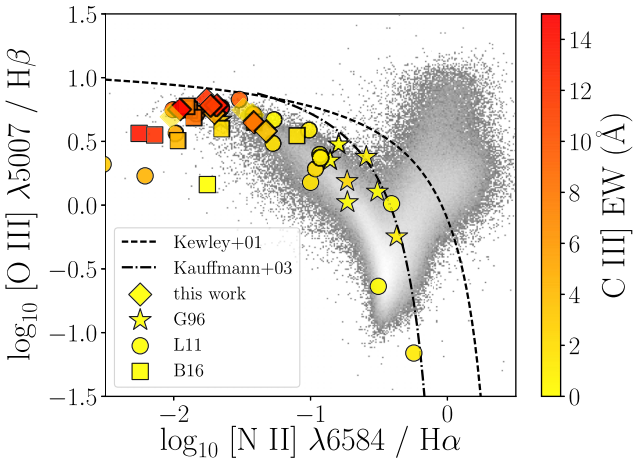

Figure 8. The BPT diagram with colour indicating the measured C III] EW for our sample (circles) and local predominantly star-forming galaxies from the literature observed with *IUE* (Giavalisco et al. 1996, G96), *FOS* (Leitherer et al. 2011, L11) and *COS* (Berg et al. 2016, B16). The grey-scale log-histogram in the background represents all local SDSS galaxies with S/N > 3 in the relevant lines. It is apparent that on average, the highest C III] EWs occur in systems in the extreme upper left, where [O III]/Hβ is maximized and [N II]/Hα is minimized, corresponding to highly ionized, lower-metallicity systems.

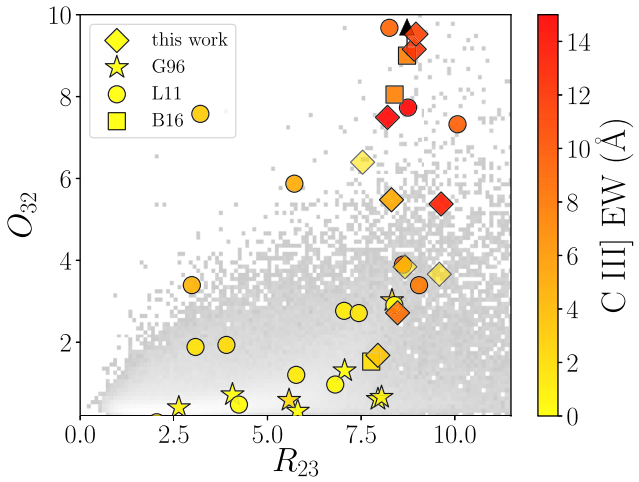

Figure 9. The O_{32}–R_{23} diagram, with symbols as in Fig. 8. Like the BPT diagram, these line ratios perform surprisingly well at separating the most extreme C III] EWs; these occur in the upper right where both the ionization parameter (O_{32}) and collisional excitation (due to inefficient cooling) are maximized.

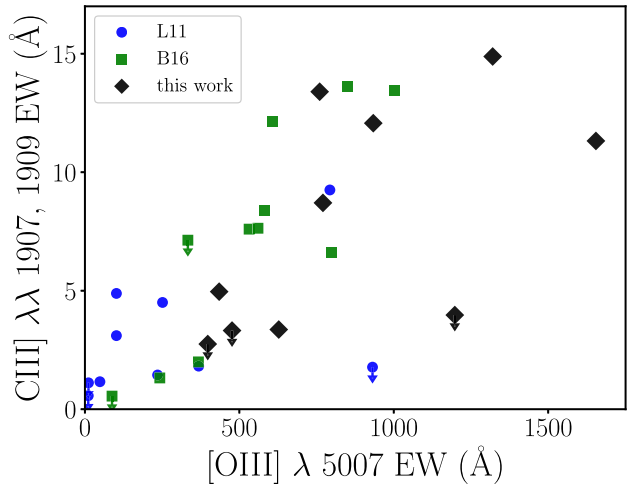

Figure 10. Equivalent width of the combined C III] λλ1907, 1909 doublet plotted against [O III] λ5007 equivalent width measured in matched SDSS spectra. In addition to the *HST*/*COS* data presented in this paper, we plot archival data from nearby galaxies catalogued by Leitherer et al. (2011, L11) and Berg et al. (2016, B16). This plot reveals a correlation between the equivalent widths of these lines, and implies that selecting galaxies based on optical [O III] equivalent width may be an efficient way to find strong UV line emitters.

below a fifth-solar, and the highest equivalent width in C IV (11 Å combined) is attained at $12 + \log \mathrm{O/H} \simeq 7.44$. This implies that the ionizing flux (and in the case of C IV, high electron temperatures) necessary to power these lines is not present above a fifth solar; see Section 5.2 for further discussion. We are currently limited by a small number of statistics in this extremely metal-poor regime. However, the present detections suggest that very strong >10 Å C IV emission may require even lower metallicities, $Z/Z_{\odot} \lesssim 1/10$.

The strength of C III] emission is clearly not a function of only metallicity. The BPT diagram probes both the gas composition and the incident ionizing spectrum, which allows for a more nuanced separation of objects than metallicity alone. In Fig. 8, we plot our objects alongside the archival sample (Appendix B) on the BPT diagram, coloured according to observed restframe C III] equivalent width. The R_{23}–O_{32} diagram separates galaxies in a similar way, but with greater sensitivity to the ionization state of the gas uncoupled from abundances. The upper right of this diagram corresponds to high ionization parameter (high O_{32}) and moderately metal-poor gas at high temperature (high R_{23}, peaking around $12 + \log \mathrm{O/H} \sim 8.0$–$8.5$; e.g. Kobulnicky, Kennicutt & Pizagno 1999; Dopita et al. 2000). We plot these line ratios for our data and the comparison sample in Fig. 9. In both diagrams, we see that strong C III]-emitters systematically populate the regions corresponding to highly ionized metal-poor gas. The objects with C III] equivalent widths above >10 Å have median $\log$ [N II]6584/H$\alpha = -1.8$ and $\log$ [O III]5007/H$\beta > 0.55$ (median 0.75), placing them securely in the extreme upper-left tail of the star-forming sequence in the BPT diagram. Similarly, these systems present median $R_{23} = 8.8$ and $O_{32} > 3.8$ (median 7.8), indicative of a substantially more ionized medium than typical in nearby galaxies (cf. the SDSS grey-scale histogram in Figs 8 and 9).

The equivalent width of [O III] emission in the optical also appears to correlate strongly with C III] equivalent width in these local galaxies. In Fig. 10 we plot C III] doublet equivalent widths against the equivalent width of [O III] λ5007. The [O III] λ5007 EWs are measured from SDSS spectra only to enforce aperture consistency – thus this plot only includes systems for which an SDSS spectrum with pointing matched to within 2 arcsec of the *COS*/*FOS* pointing was available. In these local metal-poor galaxies, C III] emission at >5 Å only occurs in galaxies with extreme optical line emission, with [O III] λ5007 equivalent width $\gtrsim$500 Å. In addition, this plot suggests a rising trend beyond even this cut-off, with galaxies above $\gtrsim$750 Å in 5007 displaying typical C III] equivalent widths ∼10–15 Å. Equivalent widths of this magnitude are extremely rare in the local universe out to $z \sim 1$, found only in low-mass systems with very high sSFR (e.g. Cardamone et al. 2009; Amorín et al. 2015).

These empirical correlations paint a clearer picture of the factors which govern UV metal line production. Exciting the UV lines requires the presence of massive hot stars capable of providing the necessary ionizing flux, and is thus associated with very recent

star formation. Above half-solar metallicity, some combination of efficient gas cooling and inefficient production of hard $\gtrsim$25 eV photons prevents C III] from reaching equivalent widths >5 Å. As a result, strong (>10 Å) C III] emitters have optical line signatures indicative of metal-poor, highly ionized gas. This is supported by detailed photoionization modelling focusing on C III], which show a similar metallicity threshold (Jaskot & Ravindranath 2016). The high electron temperatures and ionizing flux $\gtrsim$50 eV necessary to power nebular C IV and He II appears to require even more metal-poor stellar populations and gas, below a fifth-solar metallicity.

Understanding in detail how various physical parameters influence UV line equivalent widths is critical for predicting and understanding the spectra of distant populations. Two additional factors complicate interpretation of C III] in particular. First, the strength of C III] relative to O III] is related directly to the C/O ratio since both have similar ionization and excitation potentials. Due to some form of (pseudo)secondary production and release of carbon, C/O is found to correlate with O/H such that low-metallicity systems have systematically low C/O (e.g. Garnett et al. 1995; Berg et al. 2016). As expected for such metal-poor galaxies, photoionization modelling of our galaxies indicates systematically sub-solar C/O, ranging from $-0.5 \geq \log \mathrm{C/O} \geq -1.4$ (Section 3.3). In addition, the strength of C III] is further modulated by the ionization state of carbon: if sufficient flux is available above 47.9 eV, carbon may be triply ionized in quantities sufficient to weaken C III] emission.

The scatter in C III] equivalent width at fixed metallicity observed in our sample is well explained in this context, as we illustrate for the most prominent outliers. First consider SB 111, the lowest metallicity system (see Fig. 4 and Table 8). The C III] doublet is undetected, but nebular O III] is present as well as C IV, consistent with both a low C/O ratio ($\log \mathrm{C/O} = -1$; see Table 9) and highly ionized carbon. Secondly, SB 36 presents a drastically different UV spectrum from SB 82 despite being at the same gas-phase metallicity. In SB 82 we see prominent C III] (12 Å) as well as nebular He II and C IV, whereas C III] in SB 36 is relatively weak (∼5 Å) and the only other UV line detected is O III]. Though both have very high sSFR, SB 82 has a higher [O III] λλ4959, 5007 equivalent width (1300 Å compared to 600 Å) and stronger H β (180 Å versus 90 Å). This suggests that the very recent star formation history in SB 82 has produced a somewhat more dominant population of massive stars in this galaxy, reflected in the substantially different UV nebular spectra.

In contrast with the trends described above, two galaxies in our sample with relatively metal-rich gas (SB 191 and 179, $Z/Z_\odot \sim 1/3$) present large C III] equivalent widths (>5 Å). In addition to their high [O III] equivalent widths (SB 191 has the highest in our sample, with [O III] λλ4959, 5007 together reaching 2400 Å), these two systems have prominent broad stellar wind features in the UV (He II emission and C IV P-Cygni; see Fig. 4). As we will discuss further in Section 5.3, this suggests that WR stars at moderately low metallicity ($\sim Z_\odot/3$) are capable of powering strong $\gtrsim$10 Å C III] emission. These systems present the highest C III] equivalent widths at their metallicities, very close to the empirical cut-off discussed above (see Fig. 7). Such extreme stellar He II λ1640 equivalent widths (>3 Å) are rare in the local universe (Wofford et al. 2014), and the range of C III] equivalent widths systems in this state can power is presently unclear.

The empirical correlations we have discussed above have significant implications for reionization-era galaxies observed in deep rest-UV spectra. Consider EGS-zs8-1, an extremely bright $3 \times L^*_{\mathrm{UV}}$ galaxy selected by IRAC broad-band colour indicative of high equivalent width [O III]+H β and confirmed to lie at $z = 7.73$ via Lyα (Oesch et al. 2015; Roberts-Borsani et al. 2016). A deep Keck/MOSFIRE spectrum of this object revealed strong C III] emission at 22 Å equivalent width (Stark et al. 2017). At $z = 1-3$, typical massive $\sim L^\star$ star-forming galaxies emit in C III] at the $\sim 1-2$ Å level, with the most extreme Lyα emitters ($W_{0,\,\mathrm{Ly}\alpha} > 20$ Å) reaching C III] ∼5 Å (e.g. Shapley et al. 2003; Du et al. 2017). Photoionization modelling and the bulk of local star-forming galaxies suggest that C III] equivalent widths $\gtrsim$15 Å are only attained below $Z/Z_\odot \lesssim 1/5$ (Fig. 7). Indeed, stellar population synthesis modelling applied to EGS-zs8-1 indicates that this system requires a very low metallicity of $Z/Z_\odot = 0.11 \pm 0.05$. However, the surprising detection of C III] at ∼10 Å alongside extreme stellar He II emission and strong [O III] at $Z/Z_\odot \sim 1/3$ presented here opens the possibility that short-lived massive stars at higher metallicity may also be capable of powering comparable emission in systems with particular high sSFR. As we discuss further in Section 5.3, uncertainties in the evolutionary channels producing these stars and in their emergent ionizing spectra have significant consequences for physical quantities like metallicities inferred from photoionization modelling of UV lines.

While C III] emission approaching reionization-era detections has been found in local systems, no nearby star-forming galaxies have yet been found with C IV comparable to the ∼20–40 Å emission found at $z > 6$. There are now two detections of nebular C IV in the reionization era (Stark et al. 2015b; Mainali et al. 2017). These systems are gravitationally lensed and lower mass ($\sim 10^8$ M$_\odot$) than bright unlensed systems like EGS-zs8-1. On the basis of the trends discussed above and in Section 5.2, and one detection of >10 Å C IV at yet lower metallicities, this emission may be associated with extremely low-metallicity gas and stars below a tenth solar metallicity. *HST*/*COS* programs targeting very metal poor ($Z/Z_\odot < 1/10$) galaxies (e.g. GO:13788, PI: Wofford; GO:14679, PI: Stark) will be essential to establishing this, and identifying the stellar populations and conditions capable of powering this extreme C IV emission.

We have uncovered a variety of optical indicators which distinguish strong UV line emitters. The high prevalence of extreme [O III]+H β emission inferred from IRAC excesses at $z > 6$ (e.g. Labbé et al. 2013; Smit et al. 2014) suggests that these rest-UV lines are far more common in the reionization era than at lower redshift, which has already been borne out in the first deep spectroscopy of galaxies in this era. These indicators may be of significant utility in locating UV line emitters at $z \sim 2$ as well, where increasingly large samples of rest-optical spectra are being assembled (e.g. Steidel et al. 2014; Shapley et al. 2015; Kashino et al. 2017). For the highest redshifts $z > 12$ where the rest-optical is inaccessible to the *James Webb Space Telescope* (*JWST*), the rest-UV lines may be our only tools. At all redshifts, high-ionization UV lines provide an extremely sensitive probe of the ionizing spectrum which powers them.

5.2 The ionizing spectrum

The sudden appearance of high-ionization nebular emission with decreasing metallicity discussed above suggests a significant transition in the ionizing spectrum. Triply-ionizing carbon to allow nebular C IV emission requires 47.9 eV photons, and nebular He II λ1640 and λ4686 are recombination lines powered by photons beyond the He^+ ionizing edge at 54.4 eV. Direct observation of the extreme-UV (∼10–100 eV) output of massive O stars is essentially impossible at any metallicity due to the weak emergent flux and heavy attenuation by nascent gas towards these stars. High-ionization nebular emission thus potentially provides one of the only windows into the ionizing spectrum of metal-poor young stellar populations.

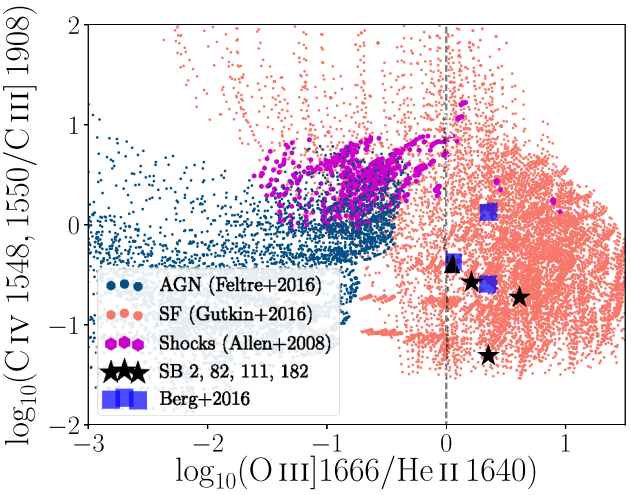

Figure 11. A line diagnostic diagram incorporating all of the high-ionization UV lines. The background circles are photoionization models powered by AGN (dark blue; Feltre et al. 2016), stellar (salmon; Gutkin et al. 2016) and shock (fuchsia, shock and precursor; Allen et al. 2008) spectra with fixed solar C/O abundance. The four metal-poor systems presented in this paper with detections of both nebular He II and C IV are plotted as black stars (or, in the case of SB 111, as a lower-limit caret corresponding to the C III] upper limit). Three similar systems from Berg et al. (2016) with *COS* detections of all four lines are plotted as blue squares. The ratios of O III]/He II are inconsistent with any AGN models – all have more flux in O III] 1666 than in He II 1640.

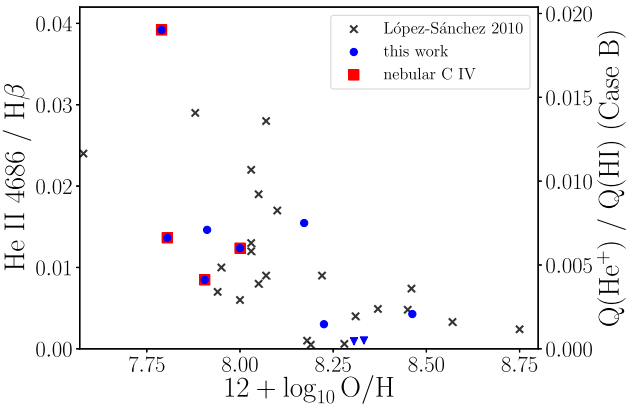

Figure 12. Measured nebular He II 4686/H β values (a proxy for the ratio of He^+-ionizing to H-ionizing photons) versus gas-phase metallicity. Both our galaxies (blue circles, backed by red squares if nebular C IV was detected) and the WR galaxies presented by López-Sánchez & Esteban (2010) are presented. The right axis indicates the corresponding $Q(He^+)/Q(H)$ assuming Case B recombination for both species. Both observational samples show a sharp transition with metallicity, with substantially larger ratios and harder spectra below $12 + \log O/H \sim 8$.

The ratios of high-ionization lines provide powerful constraints on the shape of the ionizing continuum. Photoionization modelling suggests that UV line diagnostic diagrams are useful tools for differentiating stellar from AGN ionization and potentially for inferring metallicity (Feltre, Charlot & Gutkin 2016; Gutkin, Charlot & Bruzual 2016), especially at low metallicities where traditional optical line diagnostics can fail to separate AGN from highly ionized star-forming regions (e.g. Groves, Heckman & Kauffmann 2006). However, empirical constraints on the precise diagnostic line space populated by star-forming galaxies are lacking due to the rarity of multiple UV line detections. In Fig. 11, we plot the ratios C IV/C III] and O III 1666 / He II for the four systems from our sample with detected C IV and He II alongside photoionization models from Feltre et al. (2016) for AGN and Gutkin et al. (2016) for star-forming galaxies. In addition, we plot photoionization predictions for fast radiative shocks (see Section 5.3.2) from Allen et al. (2008, shock plus precursor), which span a range of shock velocities 100–1000 km s^{-1} and metallicities down to 30 per cent solar. We also include measurements of the three extreme galaxies from Berg et al. (2016) with detected nebular C IV and He II. The position of our observations on this diagram falls within the locus of star-forming models. The hard break in the stellar spectrum beyond the He^+ ionizing edge, absent from the flatter power-law spectra yielded by AGN and radiative shocks, produces a clear separation in O III]/He II (Feltre et al. 2016; Mainali et al. 2017). All of our observations lie to the star-forming side of this division, with O III] λ1666 comparable or much stronger than He II λ1640. Similar bulk agreement with the stellar photoionization predictions is achieved in a plot of C IV/He II against O III]/He II. The disjoint position of our objects with respect to the AGN and shock models strongly implies that the nebular C IV and He II we observe are primarily powered by stellar photoionization.

The deep ESI spectra we obtained also provide constraints on the shape of the ionizing spectrum between 10 and 50 eV. The ratio of flux between the nebular He II and H recombination lines is closely related to the ratio of He^+-ionizing (<228 Å) to H-ionizing photons (<912 Å). The optical He II λ4686 and H β lines are ideal for avoiding the uncertainties introduced by dust and aperture corrections. Our ESI spectra easily resolve the nebular and broad components of the He II line (see Fig. 5) and thus allow a robust simultaneous fit to both, to which H β in the same spectrum can be compared (Section 3.4 and Table 10). The (dust-corrected) ratio of nebular He II/H β is plotted as a function of gas-phase metallicity in Fig. 12. In addition to the sample presented here, we plot the published measurements of this ratio for the local WR galaxies analysed by López-Sánchez & Esteban (2010). The axis on the right displays the ratio $Q(He^+)/Q(H)$ assuming ideal Case B recombination proceeds for both H and He^+ (and 10^4 K, 10^2 cm^{-3}; Hummer & Storey 1987; Draine 2011). The Case B predictions should be treated with care as collisional excitation and low ionization parameters can result in deviations from this assumption (e.g. Stasińska & Izotov 2001; Raiter, Schaerer & Fosbury 2010), but demonstrate clearly the effect of changing the ionizing spectrum slope at the He^+ ionizing edge.

The nebular He II/H β ratio reveals a sharp transition in the ionizing spectrum with decreasing metallicity. The maximum value of He II/H β increases as the gas-phase metallicity decreases, with a marked upturn in this envelope around $12 + \log O/H \sim 8.0$–8.2. Systems below $12 + \log O/H < 8.2$ ($<Z_\odot/3$) reach relative nebular He II fluxes nearly 10 times higher than those above this metallicity. This implies an order of magnitude increase in $Q(He^+)/Q(HI)$ as the metallicity of a young stellar population is decreased from $Z_\odot$ to $Z_\odot/10$. A similar trend towards higher He II/H β below $12 + \log O/H < 8.0$ was found in the full sample of SDSS spectra analysed by Brinchmann et al. (2008b) and Shirazi & Brinchmann (2012), though we find a far more pronounced transition. This may be due in part to confusion of strong stellar He II for nebular emission in SDSS – our higher-resolution ESI spectra revealed that both SB 179 and 191 have purely stellar emission in this line. This increase in He II/H β mirrors the transition we noted in the UV spectra, with the only nebular C IV detections occurring below $\lesssim Z_\odot/5$. A trend towards more highly ionized gas is also seen in the flux ratio of

He II λ4686 / He I λ4713 visible in Fig. 5, which increases from $\lesssim$1 in the four most metal-rich objects to $\gtrsim$2 (up to 8 in SB 111) below $12 + \log \mathrm{O/H} < 8.2$.

Our selection method complicates interpretation of Fig. 12, but does not easily explain the observed transition. Both our sample and that of López-Sánchez & Esteban (2008) were selected to show emission at He II λ4686 (in the latter case, broad stellar rather than nebular; Schaerer, Contini & Pindao 1999). We are thus biased towards higher He II/H β than a He II-blind sample. There is no clear reason why we would be biased against finding any objects in the upper-right part of of Fig. 12 – that is, with high nebular He II/H β and $12 + \log \mathrm{O/H} > 8.2$. It is possible that strong nebular and stellar He II were partially blended for some moderately metal-poor objects in SDSS, yielding very high He II/H β values and resulting in an AGN classification in SB2012. However, classification as an AGN in the SB2012 scheme required the identification of AGN-like features such as broad Balmer lines, strong Ne V λ3426, Fe II emission, or an unusual [O III] λ4363/Hγ ratio in the SDSS data as well. Regardless, future work targeting galaxies without considering He II emission in selection will enable a more complete study of this emission as a function of metallicity (e.g. HST GO:14679, PI: Stark).

There is significant tension between these results and commonly used stellar population synthesis models. Shirazi & Brinchmann (2012) found that both STARBURST 99 (Leitherer et al. 1999, 2010) and BPASS (Eldridge & Stanway 2009) can reproduce nebular He II/H β ratios as high as 1–10 per cent for instantaneous bursts of star formation, but only for a short period of time approximately 3 Myr after the burst; and only above $Z/Z_\odot > 1/5$. This modelling suggests that strong nebular He II should occur only when WR stars are active, and that large WR populations should power strong He II/H $\beta \gtrsim 1$ per cent. This is in contrast to the observations, where nebular He II is commonly seen in systems without WR features at low metallicity (Fig. 5; see also Brinchmann et al. 2008b; Shirazi & Brinchmann 2012). At the relatively high-metallicity end ($12 + \log \mathrm{O/H} > 8.1$) where strong WR features are seen, our high-resolution view of He II reveals that nebular He II is consistently weaker than predicted (He II λ4686/H $\beta < 1$ per cent). As discussed in Section 4, fits to the UV spectra presented here indicate that the prominent nebular He II λ1640 emission visible in SB 111, 2 and 182 cannot be fit with the models of Gutkin et al. (2016) without simultaneously invoking $M_{\rm up} = 300\,\mathrm{M}_\odot$ and metallicity substantially lower than the optically derived gas-phase metallicity. If we are to accurately interpret high-ionization emission in distant galaxies, we must understand the origin of these discrepancies.

5.3 Sources of ionizing radiation

Accurate predictions for extreme ultraviolet (EUV) ionizing flux from star-forming galaxies are critical for modelling and interpreting the high-ionization UV nebular lines that this flux powers. As discussed above, current stellar population synthesis models do not reproduce the strong metallicity dependence observed in He II/H β near $Z/Z_\odot \sim 1/4$ (Fig. 12). Our data reveal a sharp transition in this ratio consistent with an order of magnitude increase in $\mathrm{Q(He^+)/Q(HI)}$ as gas-phase metallicity is decreased from $Z_\odot$ to $Z_\odot/5$ (Section 5.2). Identifying the physical origin of this transition will help direct adjustments or additions to these models.

Our deep moderate-resolution *HST*/*COS* and ESI data allow us to put direct constraints on the massive stellar populations and other ionizing sources potentially present in these systems. By virtue of their selection using He II diagnostics (see Section 2.1 and Shirazi & Brinchmann 2012) and as inferred from sensitive UV line diagnostics (Fig. 11), an AGN contribution to photoionization is highly unlikely in these systems. This leaves three primary ionizing sources which could contribute to the high-ionization emission lines, which we discuss in turn: stars, fast radiative shocks and X-ray binaries.

5.3.1 *Stars*

The EUV flux output from young stellar populations which powers high-ionization nebular emission lines is very uncertain and intimately linked to stellar winds. Both OB stars and their hydrogen-stripped relatives WR stars drive winds through metal line absorption in the EUV, which diminish in strength as stellar metallicity is decreased (e.g. Castor, Abbott & Klein 1975; Kudritzki et al. 1987; Crowther et al. 2002; Vink & de Koter 2005; Crowther & Hadfield 2006). The amount of EUV flux which passes through these winds to power nebular emission is decreased substantially by high-density winds and difficult to calibrate directly, especially beyond the $\mathrm{He^+}$ ionizing edge (e.g. Smith et al. 2002; Crowther & Hadfield 2006; Smith 2014). As metallicity decreases and winds weaken, WR stars will be produced less efficiently by wind-driven mass loss. However, mass transfer in binaries can efficiently remove the outer layers of a donor star, producing a hot stripped star without the need for high wind mass loss (e.g. Maeder & Meynet 1994; Eldridge, Izzard & Tout 2008; Gotberg, de Mink & Groh 2017; Smith, Gotberg & de Mink 2017). In addition, the mass gainer in a binary system may be sufficiently spun up by angular momentum transport to become fully mixed during its hydrogen burning phase, leading to quasi-chemically homogeneous evolution and similarly high effective temperatures (Maeder 1987; Yoon & Langer 2005; Eldridge & Stanway 2012; de Mink et al. 2013). If sufficient metals are available, these stars will reveal themselves in broad wind emission lines such as He II like canonical WR stars, but at low metallicities, these sources of hard ionizing radiation will be effectively invisible except for their impact on nebular emission. The efficiency of mass transfer and the effects of rotation are both likely enhanced at lower metallicities, where weaker stellar winds allow massive stars to retain their mass longer (e.g. Maeder & Meynet 2000; Eldridge & Stanway 2009; Szécsi et al. 2015). Our moderate-resolution *HST*/*COS* and ESI spectra allow us to measure stellar wind features directly, and thus ascertain whether the wind properties of the massive stars present correlate with the nebular emission we detect.

The UV spectra reveal a significant weakening in stellar wind lines with declining gas-phase metallicity (Fig. 4). The five systems above $12 + \log \mathrm{O/H} \gtrsim 8.2$ have C IV P-Cygni absorption deeper than −4 Å, whereas the feature is uniformly weaker than this for the lower-metallicity systems. Quantitatively, the trend is consistent with other local galaxies. The empirical relation derived by Crowther et al. (2006) predicts a gas-phase oxygen abundance of $12 + \log \mathrm{O/H} = 8.2$ for a P-Cygni absorption depth of −4 Å, in good agreement with our direct-T_e gas-phase metallicities. The largely monotonic decrease in the strength of this feature with decreasing gas-phase oxygen abundance is strong evidence that the stellar metallicity and thus stellar wind strengths track the gas-phase metallicity, as expected. This confirms that the systems with the strongest observed high-ionization UV emission harbor populations of very metal-poor stars in addition to hot metal-poor gas.

The five relatively high-metallicity systems show surprisingly strong WR star signatures. The stacked G160M spectra of the systems above $12 + \log \mathrm{O/H} > 8.1$ reveals very strong broad He II λ1640 emission, with equivalent width 3.4 ± 0.2 Å and

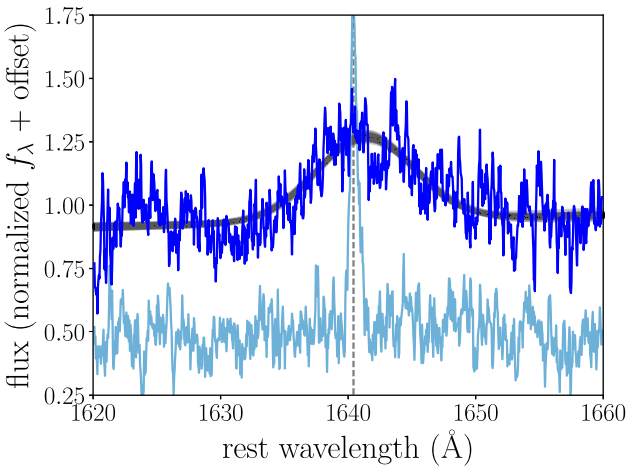

Figure 13. Stacked *HST*/*COS* spectra centred on He II 1640 for the five most metal-rich galaxies (SB 110, 179, 191, 80, 198) and the five metal-poor systems (SB 111, 2, 36, 82, 182; transparent). Samples from the MCMC Gaussian fit posterior to the metal-rich stack are overlaid in black. The moderately metal-poor stack ($12 + \log \mathrm{O/H} \gtrsim 8.1$) reveals purely broad stellar emission at extremely large equivalent width (3.4 Å). The low-metallicity stack, in contrast, is dominated by nebular emission with no obvious stellar wind contribution.

resolution-corrected FWHM 1600 km s^{-1} – easily distinguished from the purely nebular emission seen in the low-metallicity stack (Fig. 13). While the width of this feature is consistent with typical late WN-type (WNL) stars (WN6-WN8; Chandar, Leitherer & Tremonti 2004), the strength is larger than expected by common population synthesis predictions, which do not typically exceed 2 Å below solar metallicity (Brinchmann, Pettini & Charlot 2008a). Incorporating quasi-homogeneous evolution for mass gainers in binary population synthesis prescriptions enhances this wind line by producing more very hot stars capable of driving ionized winds at moderately low metallicity (Eldridge & Stanway 2012). In addition, IMF variations that allow for more very massive stars will boost this line, and may be required to explain even stronger stellar He II emission in nearby star clusters (e.g. Wofford et al. 2014). The fits presented in Section 4 are able to qualitatively reproduce the extreme stellar He II in SB 179 and 191 (Fig. 6) with the updated single-star models of Charlot & Bruzual (2017, in preparation) which incorporate an updated treatment of WR atmospheres. In any case, the prominence of broad He II emission in these systems means that massive stars at these metallicities are driving dense winds. These winds require the absorption of EUV ionizing radiation which would otherwise escape to power nebular emission.

Strong broad He II emission in our sample is accompanied by nebular emission in C III] and O III], but weak emission in higher-ionization lines. As discussed above, nebular C IV and He II are undetected in the UV above $12 + \log \mathrm{O/H} > 8.1$, where broad He II emission is detected. This is consistent with strong absorption of EUV flux in the dense winds we see in broad emission. However, at $Z/Z_\odot > 1/5$, two of the three systems with extreme stellar He II equivalent widths >2 Å show very strong C III] emission, at 9 and 11 Å (SB 179 and 191, respectively; Fig. 4). This is in striking contrast to the systems at similar metallicity but with lower equivalent width stellar He II λ1640 (SB 198 and 110), where C III] is <5 Å. While moderately metal-poor massive stars do not appear to be efficient producers of He^+-ionizing photons, this result and the archival analysis of Rigby et al. (2015) suggest that they may be an important source of the less extreme radiation necessary to produce C III]. If this alternative channel (extreme $Z/Z_\odot \sim 1/2$ massive star populations) can power emission comparable to the 22 Å equivalent width C III] detected in a massive $>L_\star$ reionization-era galaxy (Stark et al. 2017), extremely metal-poor $Z/Z_\odot < 1/10$ gas and stars may not need to be invoked (see Section 5.1). However, the efficacy of this channel is presently unclear – both SB 80 and the cluster NGC 3125-A1 analysed by Wofford et al. (2014) show >3 Å stellar He II λ1640 but undetected C III] emission, whereas NGC 5253 contains a cluster with >3 Å stellar He II and 8 Å C III] emission (Smith et al. 2016). As Smith et al. (2016) highlight, what we interpret in this paper as WR emission in He II may in some cases be produced largely by very massive H-burning stars rather than canonical He-burning WR stars – but since they drive similarly dense winds, these OIf supergiants likely present similar EUV spectra. These systems with strong stellar He II emission must have undergone very recent star formation to produce the observed massive stars. However, as discussed above, significant uncertainties in stellar evolutionary channels result in uncertain predictions for the ionizing spectrum and nebular emission from these stellar populations. Clearly, more data are required to quantify the range of C III] equivalent widths these stars can power.

The strongest nebular emission in our sample appears below $12 + \log \mathrm{O/H} < 8.1$, where stellar wind signatures vanish. Nebular C IV and He II, and the highest C III] equivalent widths in our sample (15 Å), are found in those systems where broad stellar He II emission is undetected (Fig. 4), and the ESI data reveal He II/H $\beta \gtrsim 0.01$ in these systems, systematically higher than for the more metal-rich objects (Fig. 12). The number of WR stars relative to O stars appears to decrease below this threshold (Table 10), as previously observed and predicted by population synthesis (e.g. Brinchmann et al. 2008b). Though visible WR stars become less common at low metallicities, models predict that lower metallicity stellar populations will still contain hot stripped cores produced via binary mass transfer and rotation effects (e.g. Gotberg et al. 2017). Due to declining wind densities, all of these stars are predicted to show both weaker wind lines and commensurately stronger EUV flux, especially beyond the He^+-ionizing edge – just as we infer from their nebular emission.

Our results suggest that hot stars likely dominate production of the observed nebular emission. However, we have shown that the transition to strong nebular He II and C IV may be sharper than predicted from population synthesis (Section 5.2), consistent with dense stellar winds blocking more >50 eV ionizing flux than predicted at higher metallicities. This suggests that these emission lines are potentially more useful probes of metallicity than we might have expected theoretically. Deep spectra of nearby integrated stellar populations provide one of the only windows on to the uncertain emergent ionizing spectra of metal-poor stars, with significant implications for nebular emission modelling at $z > 6$. Further work is needed to ensure that population synthesis models are able to fully reproduce the nebular and stellar features in extreme systems such as these.

5.3.2 *Fast radiative shocks*

Fast radiative shocks produced by supernovae explosions or stellar winds can provide significant EUV flux (e.g. Allen et al. 2008), but their ability to explain the nebular He II emission in these systems is unclear. Shocks are not expected to produce the strong metallicity dependence observed in the He II/H β ratio (Fig. 12). At fixed shock velocity, the resulting He II/H β ratio typically increases

with increasing metallicity, opposite the observed trend (see Izotov, Thuan & Privon 2012, using the models of Allen et al. 2008). There is no clear reason that these shocks should become more prevalent with decreasing metallicity. In addition, UV line ratios are expected to discriminate effectively between shock and stellar photoionization (e.g. Villar-Martin, Tadhunter & Clark 1997; Allen, Dopita & Tsvetanov 1998; Jaskot & Ravindranath 2016). Fig. 11 reveals that the observed UV line ratios are inconsistent with pure shock photoionization, but note that current model grids do not extend below SMC metallicities (Allen et al. 2008).

In local star-forming galaxies, shocks have been invoked primarily to explain [Ne v] λ3426 emission (e.g. Thuan & Izotov 2005; Izotov et al. 2012). The ionization potential necessary to quadruply-ionize neon is 97.1 eV, requiring photons nearly twice as energetic as for doubly ionizing helium and potentially a harder ionizing spectrum such as that provided by radiative shocks. Our MMT spectra did not reach the blue-end depth necessary to detect this line at a few per cent H β. However, SB 111 has a previously reported detection of [Ne v] emission at the $\sim 2\sigma$ level (J1230+1202 in Izotov et al. 2012). The ratio of [Ne v]/He II (0.2) is the lowest in the sample explored by Izotov et al. Though the nebular line ratios produced by shocks are predicted to be quite different from those expected by stellar photoionization, Izotov et al. (2012) found that they may explain the rare [Ne v] emission if the shock contribution to the strong lines is small and for shock velocities in the narrow range of 300–500 km/s.

With the spectral resolution provided by ESI and *HST*/*COS*, we can check directly for evidence of broad shock contributions to the optical lines. First, we do not see any evidence for the FWHM $\sim$ 1000–2000 km s^{-1} broad emission in H β and [O III] observed in some [Ne v] emitters and attributed to adiabatic shock propagation (Chevalier 1977). Though He II may be produced in the compressed pre-shock region at smaller widths, we would expect to see some broad contribution to He II and strong optical lines such as H β and [O III] at widths near the shock velocities (300–500 km s^{-1} ; Izotov et al. 2012). The He II λ4686 Å lines show no evidence for contributions besides the $\sigma < 65$ km s^{-1} nebular component and the very broad >1500 km s^{-1} stellar one (see Fig. 5). We detect broad components to H β and [O III] λ4959 in some systems, at $\sim$0.5–2 per cent of the narrow flux and with $\sigma \lesssim 300$ km s^{-1}, but these broad components show no clear correlation with the observed He II/H β ratio, and the velocity is lower than the 300–500 km s^{-1} expected from modelling of [Ne v] emitters (Izotov et al. 2012). We conclude that fast radiative shocks are unlikely to contribute substantially to the high-ionization nebular emission in these systems.

5.3.3 *X-ray binaries*

Another possible sources of hard ionizing radiation in star-forming galaxies are high-mass X-ray binaries (HMXBs), systems in which a compact object (neutron star or stellar-mass black hole) is accreting material from a massive O or B companion. Recently, a detailed study of metal-poor star-forming galaxies nearby has revealed a strong metallicity dependence in the observed hard X-ray luminosity. At fixed SFR, lower metallicity systems appear to be significantly more X-ray luminous (Prestwich et al. 2013; Brorby, Kaaret & Prestwich 2014; Brorby et al. 2016). This is likely due to some combination of weaker stellar mass loss and thus more efficient Roche lobe overflow, and more efficient mass transfer due to weaker X-ray heating of metal-poor gas (e.g. Thuan et al. 2004; Linden et al. 2010). However, archival data do not show a one-to-one correspondence between He II (or [Ne v]) and X-ray point source detections, leading other authors to conclude that HMXBs are not primarily responsible for this emission (e.g. Thuan et al. 2004; Thuan & Izotov 2005; Shirazi & Brinchmann 2012). In addition, adding HMXBs to stellar population synthesis models will generally yield a flatter ionizing continuum in the EUV (e.g. Power et al. 2013), resulting in high-ionization line ratios divergent from the stellar locus in Fig. 11.

Archival *Chandra* data are available for the most extreme nebular He II-emitter in our sample, SB 111. A *Chandra* X-ray point source was reported as associated with SB 111 ([RC2] A1228+12 by Brorby et al. (2014). We reprocessed these data following the same approach, and found that this detection is >11 arcsec (>0.9 kpc at 16 Mpc) offset from the centre of the SDSS optical fibre. No point source is detected within the $\sim$3 arcsec spectroscopic aperture to a limiting luminosity of $L_X \sim 3 \times 10^{38}$ erg s^{-1} in the 0.3–8 keV band; the reported point source cannot be responsible for the observed He II emission. More data are required to characterize the X-ray binary content of metal-poor galaxies such as these, and may additionally help constrain binary population synthesis predictions in a novel way.

6 SUMMARY

We present *HST*/*COS* UV spectra of 10 nearby galaxies with signatures of very recent star formation. The medium-resolution gratings easily disentangle nebular emission, stellar wind features, and interstellar absorption, and enable measurement of the full suite of nebular emission lines emerging in high-z rest-UV studies: C III], O III], C IV and He II (see Fig. 4). The systems are all vigorously forming stars (with sSFR of-order 100 Gyr^{-1}), yet show a remarkable diversity of UV spectral properties. Emission in the C III] semi-forbidden doublet is detected in seven objects, with equivalent widths reaching extremely high values in some cases ($\sim$10–15 Å). Systems above $Z_\odot/5$ ($12 + \log \mathrm{O/H} \gtrsim 8.0$) are dominated by stellar features, presenting strong P-Cygni absorption at C IV formed in the winds of massive O-stars and broad $\sim$1600 km s^{-1} emission in He II indicative of hot ionized winds from WR or very massive O stars. Below $Z_\odot/5$, these wind features disappear and are replaced by prominent nebular emission in both He II and C IV.

We investigate the variation in C III] equivalent width in detail. In combination with archival local samples, our data support a metallicity threshold for C III] production in star-forming galaxies, with equivalent widths >5 Å achieved only below $12 + \log \mathrm{O/H} \lesssim 8.4$ ($Z/Z_\odot \lesssim 1/2$; Fig. 7). Below this threshold, some objects reach equivalent widths comparable to those seen in reionization-era systems, while in others the doublet is undetected. This variation appears to be well-explained by variation in C/O and specific star formation rate. The hot stars and inefficient ISM cooling found below $Z_\odot/2$ appears to be required to power high-EW C III], but emission is only observed in systems with a population of very recently formed massive stars (sSFR $\gtrsim 10$ Gyr^{-1}) which can provide the necessary ionizing flux. We find that galaxies with C III] above >5 Å are associated with high [O III] λ5007 EW $\gtrsim$500 Å, [O III]λ5007/H$\beta \gtrsim 3$, and $O_{32} \gtrsim 4$ (Section 5.1). In this context, the high C III] detection rate thus far at $z > 6$ (Stark et al. 2015a; Zitrin et al. 2015; Ding et al. 2017; Stark et al. 2017) is entirely consistent with the increasingly large [O III]-H β EWs inferred from IRAC excesses (e.g. Smit et al. 2014, 2015). Both imply that the galaxies with UV metal line detections at $z > 6$ are metal-poor (confidently $Z/Z_\odot < 1/2$) and undergoing rapid star formation. We also find strong $\sim$10 Å C III] emission alongside prominent WR

signatures at $Z/Z_{\odot} \sim 1/3$. Massive stars produced in very recent bursts of star formation may be able to power extreme C III] at higher metallicity than predicted by population synthesis models, though the typical nebular output of such populations remains unclear at present.

The appearance of nebular C IV and He II below $Z/Z_{\odot} \lesssim 1/5$ implies a lower metallicity cut-off for emission in these lines. Indeed, we observe a sharp increase in the ratio of He II/H β at this metallicity, consistent with an order of magnitude increase in the hardness of the ionizing spectrum beyond the He^+-ionizing edge ($Q(He^+)/Q(H)$) below $12 + \log O/H \sim 8.0$ (Fig. 12). This transition is more rapid than predicted by stellar population synthesis models, suggesting stellar wind densities and evolutionary pathways yielding hot stripped stars may change more quickly than anticipated over this metallicity range. Our results suggest that nebular He II and C IV may prove to be useful probes of metallicity in distant galaxies, but none of our systems exceed ∼2 Å equivalent width in either. A previous detection of C IV at combined doublet EW 11 Å in a nearby star-forming system at $12 + \log O/H \sim 7.44$ (Berg et al. 2016) provides a hint that such extreme C IV may only be produced below $Z/Z_{\odot} < 1/10$. The detection of C IV at >20 Å at $z \sim 6$-7 (Stark et al. 2015b; Mainali et al. 2017) thus may indeed require extremely metal-poor gas and stars.

The *HST*/*COS* and ESI spectra acquired for our targets enable constraints to be placed on the origins of this ionizing flux. The clean transition from primarily stellar to purely nebular He II with decreasing metallicity (Fig. 5) is naturally explained by the weakening of O and WR star winds, which leads to both easier escape of >50 eV flux and to more efficient production of hot EUV-bright stars via binary mass transfer and rotation (Section 5.3). Massive stellar evolution is poorly constrained by observations in this metallicity regime, and thus high-ionization nebular emission in metal-poor dwarf galaxies is a useful window into the ionizing spectrum of these stars. While we cannot firmly rule out a contribution from shocks or X-ray binaries, these sources appear unlikely to provide the bulk of the EUV flux in these galaxies. We find no clear evidence for fast radiative shocks in high-resolution Keck/ESI spectra, and the most extreme He II-emitter has archival *Chandra* data which put a stringent upper limit on the presence of high-mass X-ray binaries.

With the growing number of high-ionization UV line detections in the reionization era, understanding how to interpret these features is becoming increasingly important. Observations at $z \sim 0$ are critical for understanding both what stellar populations power this emission and how to translate rest-UV observations at high-z into meaningful physical constraints. Our results confirm that these lines will be useful not only for redshift measurement, but as empirical probes of metallicity and star formation in the very early universe.

ACKNOWLEDGEMENTS

We thank the referee for their timely and helpful report. Based on observations made with the NASA/ESA Hubble Space Telescope, obtained from the data archive at the Space Telescope Science Institute. Support for program #14168 was provided by NASA through a grant from the Space Telescope Science Institute, which is operated by the Association of Universities for Research in Astronomy, Inc., under NASA contract NAS 5-26555. Observations reported here were obtained at the MMT Observatory, a joint facility of the University of Arizona and the Smithsonian Institution. The scientific results reported in this article are based in part on observations made by the *Chandra* X-ray Observatory and published previously in cited articles. Some of the data presented herein were obtained at the W.M. Keck Observatory, which is operated as a scientific partnership among the California Institute of Technology, the University of California and the National Aeronautics and Space Administration. The Observatory was made possible by the generous financial support of the W.M. Keck Foundation. The authors wish to recognize and acknowledge the very significant cultural role and reverence that the summit of Mauna Kea has always had within the indigenous Hawaiian community. We are most fortunate to have the opportunity to conduct observations from this mountain.

DPS acknowledges support from the National Science Foundation through the grant AST-1410155. AV, JC and SC acknowledge support from the European Research Council via an Advanced Grant under grant agreement no. 321323-NEOGAL. TJ acknowledges support from NASA through Hubble Fellowship grant HST-HF2-51359.001-A awarded by the Space Telescope Science Institute. AF acknowledges support from the ERC via an Advanced Grant under grant agreement no. 339659-MUSICOS.

This research made use of Astropy, a community-developed core Python package for Astronomy (Astropy Collaboration et al. 2013).

REFERENCES

Abazajian K. N. et al., 2009, ApJS, 182, 543
Ahn C. P. et al., 2012, ApJS, 203, 21
Allen M. G., Dopita M. A., Tsvetanov Z. I., 1998, ApJ, 493, 571
Allen M. G., Groves B. A., Dopita M. A., Sutherland R. S., Kewley L. J., 2008, ApJS, 178, 20
Amorín R. et al., 2015, A&A, 578, A105
Asplund M., Grevesse N., Sauval A. J., Scott P., 2009, ARA&A, 47, 481
Astropy Collaboration et al., 2013, A&A, 558, A33
Atek H., Kunth D., Schaerer D., Mas-Hesse J. M., Hayes M., Östlin G., Kneib J.-P., 2014, A&A, 561, A89
Baillard A. et al., 2011, A&A, 532, A74
Baldwin J. A., Phillips M. M., Terlevich R., 1981, PASP, 93, 5
Bayliss M. B., Rigby J. R., Sharon K., Wuyts E., Florian M., Gladders M. D., Johnson T., Oguri M., 2014, ApJ, 790, 144
Benjamin R. A., Skillman E. D., Smits D. P., 1999, ApJ, 514, 307
Berg D. A., Skillman E. D., Henry R. B. C., Erb D. K., Carigi L., 2016, ApJ, 827, 126 (B16)
Bitsakis T., Charmandaris V., da Cunha E., Díaz-Santos T., Le Floc'h E., Magdis G., 2011, A&A, 533, A142
Boorman P. G. et al., 2016, ApJ, 833, 245
Bouret J.-C., Lanz T., Hillier D. J., Martins F., Marcolino W. L. F., Depagne E., 2015, MNRAS, 449, 1545
Brinchmann J., Pettini M., Charlot S., 2008a, MNRAS, 385, 769
Brinchmann J., Kunth D., Durret F., 2008b, A&A, 485, 657
Brorby M., Kaaret P., Prestwich A., 2014, MNRAS, 441, 2346
Brorby M., Kaaret P., Prestwich A., Mirabel I. F., 2016, MNRAS, 457, 4081
Bruzual G., Charlot S., 2003, MNRAS, 344, 1000
Byler N., Dalcanton J. J., Conroy C., Johnson B. D., 2017, ApJ, 840, 44
Cardamone C. et al., 2009, MNRAS, 399, 1191
Castor J. I., Abbott D. C., Klein R. I., 1975, ApJ, 195, 157
Chabrier G., 2003, PASP, 115, 763
Chandar R., Leitherer C., Tremonti C. A., 2004, ApJ, 604, 153
Charlot S., Fall S. M., 2000, ApJ, 539, 718
Charlot S., Longhetti M., 2001, MNRAS, 323, 887
Chevalier R. A., 1977, ARA&A, 15, 175
Chevallard J., Charlot S., 2016, MNRAS, 462, 1415
Christensen L. et al., 2012, MNRAS, 427, 1953
Conroy C., Gunn J. E., White M., 2009, ApJ, 699, 486
Conti P. S., 1976, Memoires of the Societe Royale des Sciences de Liege, 9, 193
Crowther P. A., 2007, ARA&A, 45, 177
Crowther P. A., Hadfield L. J., 2006, A&A, 449, 711
Crowther P. A., Dessart L., Hillier D. J., Abbott J. B., Fullerton A. W., 2002, A&A, 392, 653

Crowther P. A., Prinja R. K., Pettini M., Steidel C. C., 2006, MNRAS, 368, 895
Crowther P. A. et al., 2016, MNRAS, 458, 624
Croxall K. V., Pogge R. W., Berg D. A., Skillman E. D., Moustakas J., 2016, ApJ, 830, 4
de Mink S. E., Langer N., Izzard R. G., Sana H., de Koter A., 2013, ApJ, 764, 166
de Mink S. E., Sana H., Langer N., Izzard R. G., Schneider F. R. N., 2014, ApJ, 782, 7
Dessauges-Zavadsky M., Pindao M., Maeder A., Kunth D., 2000, A&A, 355, 89
Ding J. et al., 2017, ApJ, 838, L22
Dopita M. A., Kewley L. J., Heisler C. A., Sutherland R. S., 2000, ApJ, 542, 224
Draine B. T., 2011, Phys. Interstellar Intergalactic Medium. Princeton Univ. Press, Princeton, NJ
Du X., Shapley A. E., Martin C. L., Coil A. L., 2017, ApJ, 838, 63
Eisenstein D. J. et al., 2001, AJ, 122, 2267
Eldridge J. J., Stanway E. R., 2009, MNRAS, 400, 1019
Eldridge J. J., Stanway E. R., 2012, MNRAS, 419, 479
Eldridge J. J., Vink J. S., 2006, A&A, 452, 295
Eldridge J. J., Izzard R. G., Tout C. A., 2008, MNRAS, 384, 1109
Erb D. K., Pettini M., Shapley A. E., Steidel C. C., Law D. R., Reddy N. A., 2010, ApJ, 719, 1168
Esteban C., Bresolin F., Peimbert M., García-Rojas J., Peimbert A., Mesa-Delgado A., 2009, ApJ, 700, 654
Feltre A., Charlot S., Gutkin J., 2016, MNRAS, 456, 3354
Ferland G. J. et al., 2013, RMxAA, 49, 137
Fischer C. F., Tachiev G., 2004, At Data Nucl. Data Tables, 87, 1
Fitzpatrick E. L., 1999, PASP, 111, 63
Foreman-Mackey D., Hogg D. W., Lang D., Goodman J., 2013, PASP, 125, 306
Garcia M., Herrero A., Najarro F., Lennon D. J., Alejandro Urbaneja M., 2014, ApJ, 788, 64
Garnett D. R., Kennicutt R. C. Jr, Chu Y.-H., Skillman E. D., 1991, ApJ, 373, 458
Garnett D. R., Skillman E. D., Dufour R. J., Peimbert M., Torres-Peimbert S., Terlevich R., Terlevich E., Shields G. A., 1995, ApJ, 443, 64
Giavalisco M., Koratkar A., Calzetti D., 1996, ApJ, 466, 831(G96)
Gil de Paz A. et al., 2007, ApJS, 173, 185
Giovanelli R. et al., 2007, AJ, 133, 2569
Gordon K. D., Clayton G. C., Misselt K. A., Landolt A. U., Wolff M. J., 2003, ApJ, 594, 279
Gotberg Y., de Mink S. E., Groh J. H., 2017, preprint (arXiv:1701.07439)
Groves B. A., Heckman T. M., Kauffmann G., 2006, MNRAS, 371, 1559
Guseva N. G., Izotov Y. I., Thuan T. X., 2000, ApJ, 531, 776
Gutkin J., Charlot S., Bruzual G., 2016, MNRAS, 462, 1757
Heckman T. M., Robert C., Leitherer C., Garnett D. R., van der Rydt F., 1998, ApJ, 503, 646
Huang K.-H. et al., 2016, ApJ, 817, 11
Hummer D. G., Storey P. J., 1987, MNRAS, 224, 801
Izotov Y. I., Stasińska G., Meynet G., Guseva N. G., Thuan T. X., 2006, A&A, 448, 955
Izotov Y. I., Guseva N. G., Thuan T. X., 2011, ApJ, 728, 161
Izotov Y. I., Thuan T. X., Privon G., 2012, MNRAS, 427, 1229
Izotov Y. I., Schaerer D., Thuan T. X., Worseck G., Guseva N. G., Orlitová I., Verhamme A., 2016, MNRAS, 461, 3683
James B. L., Koposov S., Stark D. P., Belokurov V., Pettini M., Olszewski E. W., 2015, MNRAS, 448, 2687
Jaskot A. E., Oey M. S., 2013, ApJ, 766, 91
Jaskot A. E., Ravindranath S., 2016, ApJ, 833, 136
Karachentsev I. D., Makarov D. I., Kaisina E. I., 2013, AJ, 145, 101
Kashino D. et al., 2017, ApJ, 835, 88
Kauffmann G. et al., 2003, MNRAS, 346, 1055
Kehrig C., Vílchez J. M., Pérez-Montero E., Iglesias-Páramo J., Brinchmann J., Kunth D., Durret F., Bayo F. M., 2015, ApJ, 801, L28
Kehrig C. et al., 2016, MNRAS, 459, 2992
Kewley L. J., Dopita M. A., Sutherland R. S., Heisler C. A., Trevena J., 2001, ApJ, 556, 121
Kewley L. J., Maier C., Yabe K., Ohta K., Akiyama M., Dopita M. A., Yuan T., 2013, ApJ, 774, L10
Kinney A. L., Bohlin R. C., Calzetti D., Panagia N., Wyse R. F. G., 1993, ApJS, 86, 5
Kisielius R., Storey P. J., Ferland G. J., Keenan F. P., 2009, MNRAS, 397, 903
Kniazev A. Y., Pustilnik S. A., Grebel E. K., Lee H., Pramskij A. G., 2004, ApJS, 153, 429
Kobulnicky H. A., Kennicutt R. C. Jr, Pizagno J. L., 1999, ApJ, 514, 544
Kojima T., Ouchi M., Nakajima K., Shibuya T., Harikane Y., Ono Y., 2017, PASJ, 69, 44
Kudritzki R. P., Pauldrach A., Puls J., 1987, A&A, 173, 293
Labbé I. et al., 2013, ApJ, 777, L19
Lee J. C. et al., 2009, ApJ, 706, 599
Leitherer C. et al., 1999, ApJS, 123, 3
Leitherer C., Ortiz Otálvaro P. A., Bresolin F., Kudritzki R.-P., Lo Faro B., Pauldrach A. W. A., Pettini M., Rix S. A., 2010, ApJS, 189, 309
Leitherer C., Tremonti C. A., Heckman T. M., Calzetti D., 2011, AJ, 141, 37
Leja J., Johnson B. D., Conroy C., van Dokkum P. G., Byler N., 2017, ApJ, 837, 170
Levesque E. M., Leitherer C., Ekstrom S., Meynet G., Schaerer D., 2012, ApJ, 751, 67
Linden T., Kalogera V., Sepinsky J. F., Prestwich A., Zezas A., Gallagher J. S., 2010, ApJ, 725, 1984
López-Sánchez Á. R., Esteban C., 2008, A&A, 491, 131
López-Sánchez Á. R., Esteban C., 2010, A&A, 516, A104
Luridiana V., Morisset C., Shaw R. A., 2015, A&A, 573, A42
Maeder A., 1987, A&A, 178, 159
Maeder A., Meynet G., 1994, A&A, 287, 803
Maeder A., Meynet G., 2000, ARA&A, 38, 143
Mainali R., Kollmeier J. A., Stark D. P., Simcoe R. A., Walth G., Newman A. B., Miller D. R., 2017, ApJ, 836, L14
Makarov D., Prugniel P., Terekhova N., Courtois H., Vauglin I., 2014, A&A, 570, A13
Massey P., 2003, ARA&A, 41, 15
Mei S. et al., 2007, ApJ, 655, 144
Merlin E. et al., 2015, A&A, 582, A15
Moustakas J., Kennicutt R. C. Jr, 2006, ApJS, 164, 81
Oesch P. A. et al., 2015, ApJ, 804, L30
Paalvast M., Brinchmann J., 2017, MNRAS, 470, 1612
Pauldrach A. W. A., Hoffmann T. L., Lennon M., 2001, A&A, 375, 161
Pérez-Montero E., Amorín R., 2017, MNRAS, 467, 1287
Power C., James G., Combet C., Wynn G., 2013, ApJ, 764, 76
Prestwich A. H., Tsantaki M., Zezas A., Jackson F., Roberts T. P., Foltz R., Linden T., Kalogera V., 2013, ApJ, 769, 92
Raiter A., Schaerer D., Fosbury R. A. E., 2010, A&A, 523, A64
Richards G. T. et al., 2002, AJ, 123, 2945
Rigby J. R., Bayliss M. B., Gladders M. D., Sharon K., Wuyts E., Dahle H., Johnson T., Peña-Guerrero M., 2015, ApJ, 814, L6
Roberts-Borsani G. W. et al., 2016, ApJ, 823, 143
Salmon B. et al., 2015, ApJ, 799, 183
Sanders R. L. et al., 2016, ApJ, 816, 23
Schaerer D., 2003, A&A, 397, 527
Schaerer D., de Barros S., 2010, A&A, 515, A73
Schaerer D., Vacca W. D., 1998, ApJ, 497, 618
Schaerer D., Contini T., Pindao M., 1999, A&AS, 136, 35
Schaller G., Schaerer D., Meynet G., Maeder A., 1992, A&AS, 96, 269
Schiavon R. P., Caldwell N., Rose J. A., 2004, AJ, 127, 1513
Schlafly E. F., Finkbeiner D. P., 2011, ApJ, 737, 103
Shapley A. E., Steidel C. C., Pettini M., Adelberger K. L., 2003, ApJ, 588, 65
Shapley A. E. et al., 2015, ApJ, 801, 88
Sheinis A. I., Bolte M., Epps H. W., Kibrick R. I., Miller J. S., Radovan M. V., Bigelow B. C., Sutin B. M., 2002, PASP, 114, 851
Shirazi M., Brinchmann J., 2012, MNRAS, 421, 1043
Smit R. et al., 2014, ApJ, 784, 58
Smit R. et al., 2015, ApJ, 801, 122
Smith N., 2014, ARA&A, 52, 487

Smith L. J., Norris R. P. F., Crowther P. A., 2002, MNRAS, 337, 1309
Smith L. J., Crowther P. A., Calzetti D., Sidoli F., 2016, ApJ, 823, 38
Smith N., Gotberg Y., de Mink S. E., 2017, preprint (arXiv:1704.03516)
Springob C. M., Masters K. L., Haynes M. P., Giovanelli R., Marinoni C., 2007, ApJS, 172, 599
Stark D. P., 2016, ARA&A, 54, 761
Stark D. P., Schenker M. A., Ellis R., Robertson B., McLure R., Dunlop J., 2013, ApJ, 763, 129
Stark D. P. et al., 2014, MNRAS, 445, 3200
Stark D. P. et al., 2015a, MNRAS, 450, 1846
Stark D. P. et al., 2015b, MNRAS, 454, 1393
Stark D. P. et al., 2017, MNRAS, 464, 469
Stasińska G., Izotov Y., 2001, A&A, 378, 817
Stasińska G., Izotov Y., Morisset C., Guseva N., 2015, A&A, 576, A83
Steidel C. C. et al., 2014, ApJ, 795, 165
Steidel C. C., Strom A. L., Pettini M., Rudie G. C., Reddy N. A., Trainor R. F., 2016, ApJ, 826, 159
Storchi-Bergmann T., Kinney A. L., Challis P., 1995, ApJS, 98, 103
Storey P. J., Sochi T., Badnell N. R., 2014, MNRAS, 441, 3028
Strauss M. A. et al., 2002, AJ, 124, 1810
Strom A. L., Steidel C. C., Rudie G. C., Trainor R. F., Pettini M., Reddy N. A., 2017, ApJ, 836, 164
Szécsi D., Langer N., Yoon S.-C., Sanyal D., de Mink S., Evans C. J., Dermine T., 2015, A&A, 581, A15
Tayal S. S., Zatsarinny O., 2010, ApJS, 188, 32
Thuan T. X., Izotov Y. I., 2005, ApJS, 161, 240
Thuan T. X., Izotov Y. I., Foltz C. B., 1999, ApJ, 525, 105
Thuan T. X., Bauer F. E., Papaderos P., Izotov Y. I., 2004, ApJ, 606, 213
Todt H., Sander A., Hainich R., Hamann W.-R., Quade M., Shenar T., 2015, A&A, 579, A75
Tonry J. L., Blakeslee J. P., Ajhar E. A., Dressler A., 2000, ApJ, 530, 625
Tully R. B., Rizzi L., Shaya E. J., Courtois H. M., Makarov D. I., Jacobs B. A., 2009, AJ, 138, 323
Vanzella E. et al., 2016, ApJ, 821, L27
Vanzella E. et al., 2017, ApJ, 842, 47
Vidal-García A., Charlot S., Bruzual G., Hubeny I., 2017, MNRAS, 470, 3532
Villar-Martin M., Tadhunter C., Clark N., 1997, A&A, 323, 21
Vink J. S., de Koter A., 2005, A&A, 442, 587
Wofford A., Leitherer C., Chandar R., Bouret J.-C., 2014, ApJ, 781, 122
Wofford A. et al., 2016, MNRAS, 457, 4296
Yoon S.-C., Langer N., 2005, A&A, 443, 643
York D. G. et al., 2000, AJ, 120, 1579
Zitrin A., Ellis R. S., Belli S., Stark D. P., 2015, ApJ, 805, L7

APPENDIX A: DISTANCES AND IDENTIFIERS

SB 2: (SDSS J094401.87-003832.1, MCG+00-25-010, CGCG 007-025, SDSS Plate-MJD-Fibre 266-51630-100) An extended BCD with at least four bright components in a linear configuration in SDSS imaging. The SDSS and *COS* spectral apertures were centred on the brightest central object. We compute a distance of 18.7 Mpc. At this distance, the *HST*/*COS* aperture radius corresponds to ∼113 pc.

SB 36: (SDSS J102429.25+052450.9, Plate-MJD-Fibre 575-52319-521) An isolated BCD with a cometary shape. We find a distance of 141 Mpc, well into the Hubble flow; at which the *HST*/*COS* aperture radius corresponds to ∼850 pc.

SB 80: (SDSS J094256.74+092816.2, Plate-MJD-Fibre 1305-52757-269) A bright H II region embedded in the warped disc of UGC 5189. We find a distance of 46.5 Mpc from the infall-corrected redshift, in good agreement with the similarly derived result of 46.4 Mpc (Baillard et al. 2011). The *HST*/*COS* aperture radius subtends 280 pc at this distance.

SB 82: (SDSS J115528.34+573951.9, Mrk 193, Plate-MJD-Fibre 1313-52790-423) An isolated BCD. We compute a distance of 75.6 Mpc, corresponding to an *HST*/*COS* aperture physical radius of ∼460 pc.

SB 110: (SDSS J094252.78+354726.0, Plate-MJD-Fibre 1594-52992-563) An isolated BCD with only a hint of extended emission beyond the bright H II region. We find a flow-corrected distance of 63.0 Mpc, at which distance the *HST*/*COS* aperture radius corresponds to ∼380 pc.

SB 111: (SDSS J123048.60+120242.8, LEDA 41360, Plate-MJD-Fibre 1615-53166-120) An isolated BCD. This cometary galaxy is dominated by a bright H II region where the SDSS spectral aperture was placed, with a much dimmer diffuse component extending to the west. It was assigned membership to the Virgo cluster by Giovanelli et al. (2007), following the group assignment procedure described by Springob et al. (2007) and the peculiar velocity model of Tonry et al. (2000). Thus, we assume the distance of the Virgo cluster, 16.5 Mpc. At this separation, the *HST*/*COS* 1.25 arcsec radius aperture probes a physical scale of order ∼100 pc.

SB 179: (SDSS J112914.16+203452.0, LEDA 35380, Plate-MJD-Fibre 2500-54178-84) A blue H II region/cluster at the south-west end of the disturbed disk galaxy IC 700. The distance of IC 700 has been estimated from the Tully–Fisher relation (typical errors of order 20 per cent) to be ∼21.5 Mpc (Bitsakis et al. 2011). Our local flow estimate provides a distance of 24.6 Mpc, in reasonable agreement with the Tully–Fisher result. We adopt the 24.6 Mpc measurement, at which distance the *HST*/*COS* aperture radius subtends ∼150 pc.

SB 182: (SDSS J114827.33+254611.7, LEDA 36857, Plate-MJD-Fibre 2510-53877-560) A BCD with a neighbouring object of similar brightness to the north-west (likely a star based on SDSS photometry). The redshift of this object suggests it is well into the Hubble flow at a distance of 191 Mpc, where the *HST*/*COS* aperture probes a region of radius ∼1.2 kpc.

SB 191: (SDSS J121518.58+203826.6, Mrk 1315, LEDA 39187, KUG 1212+209B, Plate-MJD-Fibre 2610-54476-421) A prominent H II region embedded in the southeast arm of the barred-spiral NGC 4204. A precise distance measurement is not available to this source; the Updated Nearby Galaxy Catalog provides an estimate of 8.0 Mpc based on surface fluctuations (Karachentsev, Makarov & Kaisina 2013). The Extragalactic Distance Database (Tully et al. 2009) states a preferred distance estimate of 10 Mpc based on a numerical action kinematic model. Our local flow model suggests that there is some degeneracy between this position and one consistent with the Virgo cluster – HyperLeda (Makarov et al. 2014) estimates a distance of 14.3 Mpc from the flow-corrected velocity. We adopt a distance estimate of 10 Mpc for this work. At 10 Mpc, the *HST*/*COS* aperture radius corresponds to ∼60 pc.

SB 198: (SDSS J122225.79+043404.7, SDSSCGB 20312.2, Plate-MJD-Fibre 2880-54509-277) A bright H II region embedded in the face-on spiral galaxy NGC 4301. Its velocity and position suggest that NGC 4301 is in the Virgo cluster (see also Gil de Paz et al. 2007). Thus, we adopt a distance of 16.5 Mpc. At this distance, the *HST*/*COS* aperture radius corresponds to ∼100 pc.

APPENDIX B: ARCHIVAL UV TARGETS

In order to explore the factors which control the UV line emission (and in particular that of C III]), we compare our high-sSFR sample to a larger set of local systems with UV and optical measurements in Section 5. We collect archival UV data from MAST for star-forming galaxies catalogues by Leitherer et al. (2011, *FOS* and *GHRS*; hereafter L11), Giavalisco et al. (1996, *IUE*; G96) and Berg et al.

Table B1. Archival nearby star-forming UV targets drawn from Berg et al. (2016, B16), Giavalisco et al. (1996, G96) and Leitherer et al. (2011, L11). Metallicities are as derived by the respective authors. The optical line ratio measurements are drawn from the sources referenced in the last column and dust-corrected as necessary using the Balmer decrement. All SDSS, C III], and [O III] λ5007 equivalent width measurements were made with the line-fitting technique described in Section 2.6.

Name (UV Atlas)	12 + log O/H (atlas)	C III] W_0 Å	[O III] 5007 W_0 Å (SDSS)	O_{32}	[O III] 5007 / H β	Optical source
SDSSJ025426 (B16)	8.06	1.3 ± 0.4	242 ± 13	–	4.47	SDSS
SDSSJ082555 (B16)	7.42	13.6 ± 2.4	851 ± 125	–	3.66	SDSS
SDSSJ085103 (B16)	7.66	<7.1	333 ± 19	–	3.21	SDSS
SDSSJ095137 (B16)	8.20	<53.7	53 ± 2	1.5	3.50	SDSS
SDSSJ104457 (B16)	7.44	13.4 ± 1.0	1002 ± 235	–	4.52	SDSS
SDSSJ115441 (B16)	7.75	2.0 ± 0.7	367 ± 36	–	3.97	SDSS
SDSSJ120122 (B16)	7.50	12.1 ± 0.8	606 ± 129	–	3.55	SDSS
SDSSJ122436 (B16)	7.78	7.6 ± 1.1	532 ± 65	8.1	5.61	SDSS
SDSSJ122622 (B16)	7.77	6.6 ± 1.6	798 ± 86	–	5.69	SDSS
SDSSJ124159 (B16)	7.74	8.4 ± 1.1	581 ± 157	–	4.84	SDSS
SDSSJ124827 (B16)	7.80	7.6 ± 1.1	560 ± 48	10.7	5.97	SDSS
SDSSJ141454 (B16)	7.28	<0.6	88 ± 8	–	1.45	SDSS
Haro 15 (G96)	8.57	<0.5	–	0.6	2.25	Atek et al. (2014)
IC 0214 (G96)	8.68	<1.5	–	0.7	1.27	Atek et al. (2014)
Mrk 26 (G96)	8.60	<3.7	–	0.6	1.54	Moustakas & Kennicutt (2006)
Mrk 347 (G96)	8.53	<0.5	–	0.3	1.05	Atek et al. (2014)
Mrk 496 (G96)	8.77	<1.7	–	0.4	0.57	Atek et al. (2014)
Mrk 499 (G96)	8.47	<1.4	–	0.7	2.39	Atek et al. (2014)
Mrk 66 (G96)	8.39	<0.5	–	1.3	3.00	Atek et al. (2014)
Pox 120 (G96)	7.83	13.0 ± 1.3	–	–	–	–
Pox 124 (G96)	8.28	<4.0	–	–	–	–
Tol 1924-416 (G96)	8.32	<4.9	–	3.0	4.69	Atek et al. (2014)
Tol 41 (G96)	7.98	<3.4	–	–	–	–
C1543+091 (L11)	7.80	9.2 ± 0.6	792 ± 89	9.7	5.60	SDSS
IZw18 (L11)	7.20	4.9 ± 0.9	102 ± 4	–	1.20	SDSS
IZw18-NW HIIR (L11)	7.20	3.1 ± 0.6	102 ± 5	7.6	2.09	Kehrig et al. (2016)
IZw18-SE HIIR (L11)	7.30	4.5 ± 0.6	251 ± 18	3.4	1.70	Kehrig et al. (2016)
Mrk 71 (L11)	7.90	19.5 ± 1.0	–	7.7	5.81	Moustakas & Kennicutt (2006)
NGC 1569 (L11)	8.20	<0.9	–	2.9	4.68	Moustakas & Kennicutt (2006)
NGC 2403-vs38 (L11)	8.50	1.7 ± 0.4	–	1.9	1.51	Esteban et al. (2009)
NGC 2403-vs44 (L11)	8.50	2.1 ± 0.4	–	1.9	1.93	Esteban et al. (2009)
NGC 2403-vs9 (L11)	8.10	1.8 ± 0.4	367 ± 34	–	3.06	SDSS
NGC 3690 (L11)	8.80	<0.6	10.8 ± 0.4	0.5	1.03	Moustakas & Kennicutt (2006)
NGC 4214 (L11)	8.10	<0.7	–	1.0	2.51	Moustakas & Kennicutt (2006)
NGC 4670 (L11)	8.20	1.1 ± 0.3	48.5 ± 0.9	1.2	2.36	Moustakas & Kennicutt (2006)
NGC 4861 (L11)	7.90	10.3 ± 1.2	–	3.9	5.14	Moustakas & Kennicutt (2006)
NGC 5055 (L11)	9.00	<0.7	–	–	–	–
NGC 5253-HIIR-1 (L11)	8.20	7.7 ± 0.8	–	–	–	–
NGC 5253-HIIR-2 (L11)	8.20	10.9 ± 1.8	–	–	–	–
NGC 5253-UV1 (L11)	8.30	1.9 ± 0.6	–	–	–	–
NGC 5253-UV2 (L11)	8.30	<1.8	–	–	–	–
NGC 5253-UV3 (L11)	8.30	2.1 ± 0.8	–	–	–	–
NGC 5457-NGC 5455 (L11)	8.20	<1.8	934 ± 171	2.8	3.88	Croxall et al. (2016)
NGC 5457-NGC 5471 (L11)	8.00	9.6 ± 3.1	–	7.3	6.74	Croxall et al. (2016)
NGC 5457-Searle5 (L11)	8.60	<1.2	11.5 ± 0.5	–	0.23	SDSS
NGC 7552 (L11)	9.20	1.2 ± 0.4	–	0.0	0.07	Storchi-Bergmann, Kinney & Challis (1995)
SBS 0335-052 (L11)	7.30	5.0 ± 0.3	–	–	–	–
SBS 1415+437 (L11)	7.40	5.1 ± 0.9	–	5.9	3.67	Thuan, Izotov & Foltz (1999)
Tol 1345-420 (L11)	8.00	7.8 ± 1.4	–	3.4	5.23	Dessauges-Zavadsky et al. (2000)
UM 469 (L11)	8.00	1.4 ± 0.3	235 ± 14	2.7	4.08	Kniazev et al. (2004)

(2016, *COS*; B16). We fit C III] using our line-fitting software (see Section 2.6) and adopt the gas-phase metallicity measurements from these authors. We also gather optical measurements from the literature and from SDSS for these objects where available, attempting to match the UV aperture pointings. The objects and the sources of their optical line measurements are summarized in Table B1.

In addition to the objects explicitly included in the *FOS*/*GHRS* atlas assembled by Leitherer et al. (2011), we also examine the other systems with *FOS* data presented by Garnett et al. (1995) which were excluded. These are C1543+091, 30 Doradus and SMC-N88A. The latter two are individual star-forming regions located in the LMC and SMC, respectively. Both present extremely high-equivalent width C III] emission in *FOS* spectra (29 and 43 Å).

Since the *FOS* 1 arcsec circular aperture used subtends less than a parsec at the distance of the LMC/SMC, we attribute this to aperture effects – these spectra do not include the full continuum of the ionizing sources and are thus not representative of integrated galaxy spectra, so we ignore them.

Tol 1214-277 presents clear C III] emission but the continuum is undetected, leading to a very large uncertainty in the equivalent width and an unphysically large best fit (>30 Å). We ignore it in the above analysis.

One galaxy in the Leitherer et al. (2011) sample shows potentially nebular C IV emission. We measure an equivalent width ∼25 Å in the G190H spectrum of IC 3639 (Leitherer et al. 2011), but this galaxy harbors a Compton-thick AGN (e.g. Boorman et al. 2016) which we assume is responsible for this line.

UV spectra covering C III] in nearby star-forming systems has also been taken with the Space Telescope Imaging Spectrograph (STIS) onboard HST (GO: 12472, PI: Leitherer). Measurements of C III] and metallicity for this sample were reported by Rigby et al. (2015); the highest C III] equivalent width measured therein was 8.3 Å. As these measurements have not yet been published in detail, we do not include them in our analysis, but note that they confirm the general trend displayed in Fig. 7.

Finally, note that the science apertures of these instruments vary in size dramatically. The spatial scales probed range from the 0.2-arcsec wide slit of STIS to the 10 × 20 arcsec aperture of *IUE* (with *FOS*, *GHRS* and *COS* in the 1–3 arcsec regime). As seen in the case of *FOS* spectra of clusters in the LMC and SMC (above), very small apertures at low redshift can significantly affect measured equivalent widths. While we exclude these extreme outliers from our study, a full analysis of the effect of aperture and distance differences is beyond the scope of this paper.

This paper has been typeset from a TEX/LATEX file prepared by the author.